

AJ, accepted

Uncovering Additional Clues to Galaxy Evolution. I. Dwarf Irregulars in the Field

Henry Lee^{1,2}, Marshall L. McCall^{1,3,4}, Robin L. Kingsburgh^{1,4},
Robert Ross¹, and Chris C. Stevenson^{1,3,5}

ABSTRACT

In order to recognize environmental effects on the evolution of dwarf galaxies in clusters of galaxies, it is first necessary to quantify the properties of objects which have evolved in relative isolation. With oxygen abundance as the gauge of metallicity, two key diagnostics of the evolution of dwarf irregular galaxies in the field are re-examined: the metallicity-luminosity relationship and the metallicity-gas fraction relationship. Gas fractions are evaluated from the masses of luminous components only, i.e., constituents of the nucleogenetic pool. Results from new optical spectroscopy obtained for H II regions in five dwarf irregular galaxies in the Local Volume are incorporated into a new analysis of field dwarfs with $[\text{O III}]\lambda 4363$ detections and good distances. The updated fit to the metallicity-luminosity relationship is consistent with results reported in the literature. The fit to the metallicity-gas fraction relation shows an excellent correlation consistent with expectations of the simple “closed box” model of chemical evolution. The simplest explanation consistent with the data is that flow rates are zero, although the observations allow for the possibility of modest flows. The derived oxygen yield is one-quarter of the value for the solar neighbourhood.

Subject headings: galaxies: abundances — galaxies: dwarf — galaxies: evolution — galaxies: irregular

¹Department of Physics & Astronomy, York University, 4700 Keele St., Toronto, ON, Canada M3J 1P3.

²Present location: Max-Planck-Institut für Astronomie, Königstuhl 17, D-69117, Heidelberg, Germany. E-mail: lee@mpia.de

³Visiting Astronomer, Steward Observatory, operated by The University of Arizona.

⁴Visiting Astronomer, Observatorio Astronómico Nacional (San Pedro Mártir), operated by the Instituto de Astronomía, Universidad Nacional Autonómica de México.

⁵Present location: Department of Physics & Physical Oceanography, Memorial University of Newfoundland, St. John’s, Newfoundland, Canada A1B 3X7.

1. Introduction

Dwarf galaxies make the largest contribution to galaxies by number and type (e.g., Binggeli, Sandage, & Tammann 1985; Ferguson 1989; Marzke & Da Costa 1997; Secker, Harris, & Plummer 1997; Mateo 1998; Phillipps et al. 1998; Driver & Cross 2000) and are considered to be the building blocks in hierarchical scenarios of galaxy formation. Being metal–poor, they represent the systems which have evolved least since the Big Bang. Although some dwarf galaxies are exceedingly faint, they may contain large amounts of dark matter in proportion to their luminous masses.

Dwarf irregular galaxies (dIs), which are the focus of this paper, are characterized by an irregular visual appearance, large gas reservoirs (e.g., Roberts & Haynes 1994; Hoffman et al. 1996), low dust content (e.g., see review by Calzetti 2001), a lack of distinct spiral arms, and star formation scattered throughout the body of the galaxies (see also reviews by Gallagher & Hunter 1984; Hunter & Gallagher 1986, 1989; Hunter 1997). H II regions provide a way to judge the total metallicity, because measures of oxygen abundance within these H II regions probe the most recent period of chemical enrichment (e.g., Dinerstein 1990; Shields 1990). Oxygen abundances within dIs do not vary greatly with galactocentric radius (e.g., Kobulnicky & Skillman 1996; Devost, Roy, & Drissen 1997; Kobulnicky & Skillman 1997). Blue compact dwarf galaxies (BCDs) contain very bright central H II regions. Here, dIs are chosen for study over BCDs, because the contribution of light from young stars in dIs is much less than the light from the underlying old stellar population (e.g., Thuan 1985). By contrast, dwarf ellipticals (dEs) and dwarf spheroidals (dSphs) have smoother visual appearances, mostly old stars, and low gas content. dEs and dSphs, respectively, are the bright and faint representatives of gas–poor dwarf galaxies in which star formation has ceased (e.g., Binggeli, Sandage, & Tarenghi 1984; Kormendy 1985; Bender, Burstein, & Faber 1992; Binggeli 1994). In all of these types of dwarf galaxies, central surface brightness increases with increasing luminosity⁶. It seems natural to consider a possible evolutionary relationship between dIs and dEs/dSphs (e.g., Faber & Lin 1983; Lin & Faber 1983; Bothun et al. 1986; Dekel & Silk 1986; Davies & Phillipps 1988, 1989; Ferguson & Binggeli 1994). However, it is not yet well understood how dIs could have evolved or transformed to become dEs/dSphs, as dIs have bluer colours and lower surface brightnesses than luminous dEs/dSphs at a given luminosity (e.g., Bothun et al. 1986; Davies & Phillipps 1988). Moreover, while a relationship between iron abundance in stars and galaxy luminosity has been observed in nearby dSphs (Aaronson et al. 1978; Smith 1985; Aaronson 1986; Grebel & Guhathakurta 1999; Côté et al. 2000; Prada & Burkert 2002), Richer & McCall (1995) and Richer, McCall, & Stasińska (1998) showed that oxygen abundances for a number of field dSphs are about +0.3 dex higher than in field dIs at similar luminosities and concluded that the predecessors of these nearby dSphs could not have been dIs.

Owing to their relatively low gravitational potentials, dwarf galaxies are thought to be susceptible to internal blow–out of their gaseous contents (e.g., Dekel & Silk 1986; Puche et al. 1992; Martin

⁶Low–luminosity ellipticals or LLEs (e.g., M32) are structurally similar to giant ellipticals and exhibit a trend of decreasing surface brightness with increasing luminosity.

1996; DellaCeca, Griffiths, & Heckman 1997; Strickland, Ponman, & Stevens 1997), although some claim that blow-out signatures of dwarf galaxies have not been definitively observed (Bothun, Eriksen, & Schombert 1994; Skillman 1997; Meurer 1998; Mac Low & Ferrara 1999; Ferrara & Tolstoy 2000). This motivates careful study of the chemical properties of field dIs, which have the potential to uncover the relevance of gas flows to evolution in isolation. With knowledge about the history of field dIs, it becomes possible to examine differentially the evolution of dIs in clusters, and thereby pinpoint perturbations stemming from the different environments. A subsequent comparison with the Virgo Cluster is the subject of Paper II (Lee, McCall, & Richer, in preparation).

The outline of the paper is as follows. The sample of field dwarfs is presented in § 2. Observations and reductions are described in § 3. The data analysis and a discussion of oxygen abundances are presented in § 4 and § 5, respectively. The derived properties are listed in § 6. Two key diagrams are used as diagnostics of dI evolution: the oxygen abundance versus luminosity and the oxygen abundance versus baryonic gas fraction. A discussion of these diagnostics and how the gas and stellar constituents are used to define the gas fraction is presented in § 7. Finally, the conclusions are given in § 8.

2. The Sample of Dwarf Irregulars in the Field

The sample of dIs in the field compiled by Richer & McCall (1995) is the starting point of research for this work. The sample is defined by two criteria: (1) oxygen abundances are determined directly from measurements of the $[\text{O III}]\lambda 4363$ emission line, and (2) distances are determined from stellar properties following the prescription in the appendix of Richer & McCall (1995). Table 1 lists the field sample of 22 dwarf irregular galaxies along with their basic properties. A new addition to the sample is DDO 187 (§ 2.3), which also satisfies the above criteria.

To establish the best possible parameters for the field sample, the literature was searched for measurements more recent than those compiled by Richer & McCall (1995). Direct oxygen abundances and well-determined distances were obtained from data given in papers describing emission-line spectroscopy and photometry of resolved stellar populations, respectively. Tables 2 and 3, respectively, summarize the dwarf galaxies whose distances and oxygen abundances have been updated. Of note also are updates to values of the H I 21-cm flux (Hoffman et al. 1996; Stil & Israel 2002) for GR 8, IC 1613, NGC 1569, and Sextans B.

2.1. Distances

Distance measurements founded upon the observations of Cepheid variable stars or the location of the tip of the red giant branch were preferred. Distance determinations from Cepheids are founded upon the Cepheid calibration by Madore & Freedman (1991), whose value of the distance modulus to the LMC was 18.50 mag. Panagia (1999) measured the geometric expansion of the ring

in the supernova remnant SN1987A and derived a distance modulus of 18.58 mag. This value of the distance modulus to the LMC is adopted for the remainder of this work. Values of distance moduli from Cepheids are adjusted by +0.08 mag to account for the revised distance to the LMC.

Lee, Freedman, & Madore (1993) showed that the absolute magnitude in I of the tip of the red giant branch (TRGB), M_I , is relatively constant, independent of metallicity and age, so long as the stars are generally metal–poor ($[\text{Fe}/\text{H}] \lesssim -0.7$ dex) and older than a few Gyr. Thus, measurements of M_I for resolved galaxies are good gauges of distance. To account for modest variations in colour and metallicity in each galaxy, absolute magnitudes in I of the TRGB were obtained following the prescription of Richer & McCall (1995). Distance moduli were derived from observed magnitudes in I , corrected for extinction. In spite of the dispute regarding the range in distance moduli to the LMC, it is reassuring that distances obtained from TRGB measurements (Cioni et al. 2000; Sakai, Zaritsky, & Kennicutt 2000) are consistent with and independent of the distance derived from the SN1987A measurement.

For galaxies with more than one kind of observation, derived distance moduli were averaged. Generally, the errors in distance moduli obtained from either Cepheids or the TRGB are about 0.2 mag. For the remaining galaxies in Table 1 with no recent updates in the literature since 1995, distance moduli derived by Richer & McCall are adjusted by +0.208 mag, because the value for the distance modulus to the LMC used by Richer & McCall (1995) was 18.372 mag.

2.2. Oxygen Abundances

Many authors have reported emission–line spectra of H II regions in field dIs since Richer & McCall (1995) compiled results from the literature. Oxygen abundances have been computed from these spectra using the published measurements of $[\text{O II}]\lambda 3727$, $[\text{O III}]\lambda 4363$, and $[\text{O III}]\lambda\lambda 4959, 5007$ emission lines. These updates are listed in Table 3, which also incorporates new spectroscopic data for five field dIs obtained by M. McCall at the Steward Observatory and, with R. Kingsburgh, at the Observatorio Astronómico Nacional (OAN) in México. The new data are described in § 3.

2.3. A New Addition: DDO 187

DDO 187 (UGC 9128) is an isolated late–type, gas–rich dwarf galaxy, which appears to have disk–halo structure. The disk stellar component extends much farther out than the gas component; the outer component does not contain young stars (Aparicio, Tikhonov, & Karachentsev 2000). A distance based on the measurement of two Cepheids has been determined by Hoessel et al. (1998b). However, the TRGB distance determined by Aparicio, Tikhonov, & Karachentsev (2000) is almost three times smaller than the Cepheid distance.

H II regions at the centre have been observed by Strobel, Hodge, & Kennicutt (1991), Hunter,

Hawley, & Gallagher (1993), and van Zee, Haynes, & Salzer (1997). van Zee, Haynes, & Salzer (1997) obtained spectroscopy for the two brightest H II regions; $[\text{O III}]\lambda 4363$ was detected and an oxygen abundance was determined for DDO 187–1, which is the brighter of the two H II regions. The published fluxes for DDO 187–1 were reanalyzed in a manner similar to the analysis of the five field dIs for which new spectra were acquired.

3. New Spectra: Observations and Reductions

A program of long-slit spectroscopy was carried out at the Steward Observatory and the OAN to acquire optical spectra for a number of dwarf galaxies in the field. The primary goal was to obtain sufficiently long exposures to detect the temperature-sensitive $[\text{O III}]\lambda 4363$ emission line. Results for five dIs are presented here. In each of the dIs, H II regions for which spectra were obtained were matched with identifications in the published literature; these are described below. Spectra for H II regions Holmberg II–9, NGC 1560–2, IC 10–2, NGC 3109–3, and UGC 6456–2 are shown in Figures 1 and 2. Details of the instrumentation employed and the log of observations are listed in Tables 4 and 5, respectively.

Spectra were reduced in the standard manner using IRAF⁷ routines from the long-slit spectroscopy reduction package “specred.” Dome flat exposures were used to remove pixel-to-pixel variations in response. Cosmic rays were identified and deleted manually. Final one-dimensional flux-calibrated spectra for each H II region were obtained via unweighted summed extractions.

3.1. H II Regions in Holmberg II

Several of the H II regions in Holmberg II were spanned by the long slit employed at Steward. Table 6 lists the H II regions for which spectra were acquired and in which the $[\text{O III}]\lambda 4363$ line was detected. Locations of the H II regions were determined by comparing finding charts used by M. McCall against published $\text{H}\alpha$ data (Hunter & Gallagher 1985; Hodge, Strobel, & Kennicutt 1994).

3.2. H II Regions in IC 10

Table 7 lists the H II regions for which spectra were acquired at Steward. These same data have been used previously to study the extinction in IC 10 (Richer et al. 2001). By inspection of finding charts provided by M. McCall, the locations of the observed H II regions were matched

⁷IRAF is distributed by the National Optical Astronomical Observatories, which is operated by the Associated Universities for Research in Astronomy, Inc., under contract to the National Science Foundation.

with H II regions identified by Lequeux et al. (1979) and Hodge & Lee (1990).

In addition to the Steward data, long-slit spectra between 3450 Å and 7450 Å were obtained with the 2.1-metre telescope at the OAN on 1994 December 1 (UT). Spectra were acquired specifically to measure H α and H β to provide a larger wavelength baseline for a truer estimation of the reddening. The spectra were reduced in a manner similar to the Steward data. H II regions identified at the OAN were matched with those identified at Steward, so that the appropriate reddening corrections could be applied directly to each H II region.

3.3. H II Regions in NGC 1560

The long slit was placed lengthwise along the major axis of the galaxy to obtain spectra of H II regions located in the disk. Table 8 lists the H II regions for which spectra were acquired. From inspection of finding charts, H α images provided by M. McCall, and the broadband images by Lee & Madore (1993), approximate locations of observed H II regions with respect to the measured stars in Lee & Madore (1993) were determined. The H II region NGC 1560–1 is visible as the brightest “concentration” located near the centre of the galaxy in the V -band image of Lee & Madore (1993). For H II regions NGC 1560–6 and NGC 1560–7, [O III] $\lambda 4363$ was not detected because of the poor quality of the spectra.

3.4. H II Regions in NGC 3109

Table 9 lists the H II regions for which spectra were measured. By inspection of the finding charts by M. McCall, the locations of the observed H II regions were matched with Richer & McCall (1992). A continuum-subtracted H α image may also be found in Hunter, Hawley, & Gallagher (1993, Figure 11), but it is difficult to match the H II regions in their H α image with the H II regions identified in the [O III] $\lambda 5007$ image by Richer & McCall (1992).

3.5. H II Regions in UGC 6456

The long slit was placed on the galaxy in an orientation similar to that employed by Tully et al. (1981). Table 10 lists the H II regions for which spectra were measured. By inspection of the finding charts by M. McCall, the locations of the observed H II regions were matched with Tully et al. (1981) and Lynds et al. (1998).

4. Measurements and Analysis

Emission-line strengths were measured using locally-developed software. Flux ratios were corrected for underlying Balmer absorption with an equivalent width 2 Å (McCall, Rybski, & Shields 1985). Corrections and analyses were performed with SNAP (Spreadsheet Nebular Analysis Package, Krawchuk et al. 1997).

A reddening, $E(B - V)$, was computed from Balmer flux ratios using

$$\log \frac{I(\lambda)}{I(H\beta)} = \log \frac{F(\lambda)}{F(H\beta)} + 0.4 E(B - V) [A_1(\lambda) - A_1(H\beta)]. \quad (1)$$

$F(\lambda)/F(H\beta)$ and $I(\lambda)/I(H\beta)$ are the observed flux ratio and corrected intensity ratio, respectively, at wavelength λ . $A_1(\lambda)$ is the extinction in magnitudes for $E(B - V) = 1$, i.e., $A_1(\lambda) = A(\lambda)/E(B - V)$, where $A(\lambda)$ is the monochromatic extinction in magnitudes. Values of A_1 were obtained from the Cardelli, Clayton, & Mathis (1989) reddening law as defined by a ratio of the total to selective extinction, R_V , equal to 3.07, which in the limit of zero reddening is the value for an A0V star (e.g., Vega) with intrinsic $B - V$ colour equal to zero. For $H\alpha$ - and $H\gamma$ -based reddening, the ratios $I(H\alpha)/I(H\beta) = 2.86$ and $I(H\gamma)/I(H\beta) = 0.468$ were adopted, respectively, which are appropriate for typical conditions within H II regions ($T_e = 10^4$ K and $n_e = 100$ cm $^{-3}$; Osterbrock 1989).

After correcting line ratios for the initial estimate of the reddening, the temperature was estimated and a second value of the reddening was computed. SNAP was used to compute temperatures by directly solving the equations of statistical equilibrium and determining the emissivities for collisionally excited lines of O $^+$ and O $^{+2}$ using the five-level atom approximation (see, e.g., De Robertis, Dufour, & Hunt 1990). In the absence of [O III] $\lambda\lambda 4363$, the electron temperature was assumed to be $T_e = 10^4$ K. Because the spectra acquired at Steward were obtained at wavelengths between 3600 Å and 5100 Å, the lines $H\alpha$, [N II] $\lambda\lambda 6548, 6583$, and [S II] $\lambda\lambda 6716, 6731$ were not detected. As the density-dependent line ratio, $I([S II]\lambda 6716)/I([S II]\lambda 6731)$, could not be formed, a value of $n_e = 100$ cm $^{-3}$ was adopted. It was found that the reddening values did not change significantly from the first to the second iteration. Also, the derived temperature in the second iteration was found to be very similar to the value from the first iteration.

$H\gamma$ -based reddening were used to correct spectra of H II regions in Holmberg II, NGC 3109, and UGC 6456. $H\alpha$ -based reddening were used to correct spectra of H II regions in IC 10 and NGC 1560. $F(H\gamma)/F(H\beta)$ was not used in a number of spectra (e.g., IC 10, NGC 1560) because of severe absorption or poor signal at $H\gamma$.

Observed and corrected line ratios for the five field dIs observed at Steward and at the OAN are listed in Tables 11 to 17 inclusive. The listed errors for the observed flux ratios at each wavelength λ account for the errors in the fits to the line profiles, their surrounding continua, and the relative error in the sensitivity function stated in Table 5. The error in the $H\beta$ reference line is not included in the observed ratios. The uncertainty in the correction for underlying Balmer absorption was taken to be zero. Errors in the corrected intensity ratios account for errors in the specified line and

in the $H\beta$ reference line. Brief comments about the line ratios for each dI are presented below.

4.1. Holmberg II

Observed flux and corrected intensity ratios are listed in Table 11. No variations in T_e were observed to within the computed errors. The reddening values for Holmberg II were found to be small and consistent with zero. Thus, zero reddening was adopted and the observed flux ratios were subsequently compensated only for underlying Balmer absorption with an equivalent width of 2 Å.

4.2. IC 10

Observed flux and corrected intensity ratios obtained at the OAN are listed in Table 12. Derived reddening values for each H II region are also listed. As stated in § 3.2, the OAN spectra were obtained for the purpose of deriving a reddening value from $H\alpha$ and $H\beta$ fluxes. For the Steward data, intensity ratios were derived from flux ratios by compensating for underlying Balmer absorption with an equivalent width of 2 Å and for the reddening derived for each H II region from the OAN data. Observed flux and corrected intensity ratios are listed in Table 13. Errors in the corrected intensity ratios account for errors in the flux at the specified line, errors at the $H\beta$ reference line, and errors in the reddening values from data obtained at the OAN.

Line intensity ratios for a number of H II regions IC 10 have also been reported by Richer et al. (2001). The flux ratios for IC 10–2 and IC 10–4 (Table 13) are comparable to those reported for HL111c and HL111b, respectively, which were derived independently from the same set of observations.

4.3. NGC 1560

Because NGC 1560 is at a low galactic latitude, there is expected to be non-negligible foreground extinction along the line-of-sight (Buta & McCall 1999). A second observing program at Steward was designed specifically to measure $H\alpha$ and $H\beta$ fluxes, because the $H\gamma$ fluxes were found to be unusable. The long slit was placed on the northeast and southwest regions of the galaxy, so the H II regions observed were different from those examined at blue wavelengths. Reddening values were derived from $F(H\alpha)/F(H\beta)$. An average reddening of $E(B - V) = +0.36$ mag was computed from the H II regions 1 NE, 1 SW, 2 SW, 3 SW, and 6 SW. This value was adopted to correct line ratios for H II regions observed in the blue. Line data and the reddening values are listed in Table 14.

Observed flux and corrected intensity ratios for the blue spectroscopic data are listed in Ta-

ble 15. Flux ratios for the two H II region spectra NGC 1560–1 and NGC 1560–2 are in agreement with those determined independently by M. G. Richer (personal communication) from the same set of observations.

4.4. NGC 3109

Observed flux and corrected intensity ratios are presented in Table 16. Reddening values derived from $F(\text{H}\gamma)/F(\text{H}\beta)$ were found to be near zero, consistent with the small value listed in NED. Zero reddening was adopted and the observed flux ratios were subsequently compensated only for underlying Balmer absorption with an equivalent width of 2 Å.

4.5. UGC 6456

Observed flux and corrected intensity ratios are listed in Table 17. Values of the reddening derived from $F(\text{H}\gamma)/F(\text{H}\beta)$ were consistent with zero. Zero reddening was adopted and the observed flux ratios were subsequently compensated only for underlying Balmer absorption with an equivalent width of 2 Å.

4.6. DDO 187

The fluxes reported by van Zee, Haynes, & Salzer (1997) were reanalyzed in the same manner as the five previous dIs. Zero reddening was assumed and the observed flux ratios were corrected for underlying Balmer absorption with an equivalent width of 2 Å. Observed and corrected line ratios are listed in Table 18.

5. Oxygen Abundances

The direct or standard method of obtaining oxygen abundances from emission lines is applicable to any object with detectable $[\text{O III}]\lambda 4363$ and for which the doubly ionized O^{+2} ion is the dominant form of oxygen (Osterbrock 1989). The method by which oxygen abundances are derived with the standard method is summarized in Dinerstein (1990). Computations for the present work were performed with SNAP.

Given a temperature and a density, an oxygen abundance is determined from strong emission arising from singly- and doubly-ionized oxygen. At temperature T_e , the relative abundances of singly- and doubly-ionized oxygen by number are, respectively,

$$\frac{N(\text{O}^+)}{N(\text{H})} = \frac{I([\text{O II}]\lambda 3727)}{I(\text{H}\beta)} \cdot \frac{j(\text{H}\beta; n_e, T_e)}{j([\text{O II}]\lambda 3727; n_e, T_e)}, \quad (2)$$

$$\frac{N(O^{+2})}{N(H)} = \frac{I([O\ III]\lambda 5007)}{I(H\beta)} \cdot \frac{j(H\beta; n_e, T_e)}{j([O\ III]\lambda 5007; n_e, T_e)}, \quad (3)$$

where I is the intensity of the line at wavelength λ , j is the volume emissivity of the line at density n_e and temperature T_e , and $N(A^{+k})$ is the abundance by number of the atomic species in the k th-ionized state responsible for the line. Data for Balmer line emissivities were taken from Storey & Hummer (1995). Emissivities for neutral and ionic oxygen were computed using spontaneous emission coefficients from Wiese et al. (1996) and collision strengths from various sources (Pradhan 1976; McLaughlin & Bell 1993; Lennon & Burke 1994; Bhatia & Kastner 1995). The total oxygen abundance by number, $N(O)/N(H)$, is obtained from the sum

$$\frac{N(O)}{N(H)} = f \cdot \left[\frac{N(O^+)}{N(H^+)} + \frac{N(O^{+2})}{N(H^+)} \right], \quad (4)$$

where f is an ionization correction factor to account for unobserved oxygen ions. Since there was little or no He II emission, the ionization correction factor could be assumed to be unity.

6. Derived Properties

Derived properties for the five dIs observed at Steward and San Pedro Mártir are listed in Table 19. For at least one H II region in each of Holmberg II, IC 10, NGC 3109, and UGC 6456, $[O\ III]\lambda 4363$ was detected and an oxygen abundance was derived directly. A meaningful lower limit to the oxygen abundance was obtained for NGC 1560. The listed properties include $H\beta$ intensities corrected for underlying Balmer absorption and reddening, derived and adopted values of the reddening, $H\beta$ emission equivalent widths corrected for underlying Balmer absorption, O^{+2} electron temperatures, and resulting oxygen abundances. Errors in oxygen abundances were computed from the maximum and minimum possible values, given the errors in the reddening, temperature, and line intensities.

6.1. Holmberg II

Oxygen abundances for H II regions Ho II–5, Ho II–8, and Ho II–9 were adopted, because these H II regions are independent of each other and have the largest $H\beta$ intensities. The abundance for Ho II–7 was not adopted, because the corresponding spectrum encompasses the spectra of both Ho II–6 and Ho II–8 (see Table 6). Oxygen abundances for three H II regions reported by Masegosa, Moles, & del Olmo (1991) were re-analyzed in the same manner as the Steward data. The average oxygen abundance listed in Table 1 was computed using results for the three selected H II regions in the present analysis and results for the three H II regions in Masegosa, Moles, & del Olmo (1991).

6.2. IC 10

Oxygen abundances for H II regions IC 10–2 and IC 10–3 were adopted. The abundance for IC 10–1 was not adopted, because the extracted spectrum encompasses the spectra for IC 10–2 and IC 10–3 (see also Table 7). The oxygen abundance for IC 10 listed in Table 1 is an average of abundances for IC 10–2 and IC 10–3. Computed errors in derived oxygen abundances include errors in both reddenings and temperatures. For IC 10–2, the derived oxygen abundance ($12+\log(\text{O/H}) = 8.32 \pm 0.14$) agrees with the value independently derived by Richer et al. (2001) for the same Steward data, but is just outside of the value published by Lequeux et al. (their H II#1; 1979).

6.3. NGC 1560

The $[\text{O III}]\lambda 4363$ line was not detected. To determine a lower limit to the oxygen abundance for the galaxy, two spectra with the highest signal-to-noise were selected from the seven H II regions observed. For H II regions NGC 1560–1 and NGC 1560–2, the lower limits are $12+\log(\text{O/H}) \geq 8.05$ and ≥ 7.89 , respectively. The mean of lower limits is a lower limit to the mean, provided that each lower limit is lower than the true abundance values (Richer & McCall 1995). So, the mean of the lower limits obtained from the present analysis was $12+\log(\text{O/H}) \geq 7.97$, which was adopted as the lower limit to the oxygen abundance for NGC 1560.

6.4. NGC 3109

In H II region NGC 3109–3, $[\text{O III}]\lambda 4363$ was detected, from which an oxygen abundance of $12+\log(\text{O/H}) = 7.73 \pm 0.33$ was derived. The oxygen abundance for NGC 3109 listed in Richer & McCall (1995), which was derived from the same Steward data, is 1σ higher than the present value. The ratio $F([\text{O III}]\lambda 4363)/F(\text{H}\beta)$ for NGC 3109–3 is $(5.73 \pm 2.04)\%$; the measurement has an error of 36%. It is worth noting that the value of the oxygen abundance given in Richer & McCall (1995) is based upon a previous coarse analysis of the same Steward data in which $[\text{O III}]\lambda 4363$ was not measured with a high degree of confidence. From M. G. Richer (personal communication), their $F([\text{O III}]\lambda 4363)/F(\text{H}\beta)$ was $(3.13 \pm 1.49)\%$ with a measurement error of 48%. The improvement here was due to an improvement in the procedure used to extract the H II region spectrum. The new value of the oxygen abundance was adopted for NGC 3109 and listed in Table 1. The error in the adopted oxygen abundance is large (0.33 dex), because of significant errors ($\simeq 10\%$) in each of the corrected intensity ratios for $[\text{O II}]$ and $[\text{O III}]$, as well as an error near 40% in the corrected intensity ratio for $[\text{O III}]\lambda 4363$.

6.5. UGC 6456

The oxygen abundance for the brighter H II region UGC 6456–2 ($12+\log(\text{O/H}) = 7.45$) was adopted for the present work. Izotov, Thuan, & Lipovetsky (1997), Lynds et al. (1998), and Hunter & Hoffman (1999) provide more recent measurements. A homogeneous treatment of these data gives oxygen abundances of $12+\log(\text{O/H}) = 7.65$, 7.74, and 7.73, respectively. The oxygen abundance for UGC 6456 listed in Table 1 is an average of the abundance derived here and abundances from the three measurements in the literature.

6.6. DDO 187

For DDO 187, the derived values for the electron temperature and oxygen abundance agree with the results in van Zee, Haynes, & Salzer (1997). From the present analysis, an oxygen abundance of $12+\log(\text{O/H}) = 7.69 \pm 0.09$ is derived for DDO 187–1.

7. The Evolution of dIs in the Field

An understanding of the properties and their correlations for a sample of dIs in the relatively low density environment of the field is required to explore and discern possible differences for galaxy evolution in high density environments. The metallicity–luminosity (O/H vs. M_B) and the metallicity–gas fraction (O/H vs. μ) diagrams are key diagnostics of evolution.

7.1. Fitting Procedure

A best-fit line for the correlation between two parameters with comparable errors is obtained with the geometric mean functional relationship (Draper & Smith 1998), which assumes similar dispersions in both observables. The geometric mean functional relationship relies upon the minimization of the sum of areas bounded by the shortest horizontal and vertical lines from each data point to the best-fit line. While maximum likelihood techniques are more appealing for best results, these methods do not work as well when the datasets are small (Draper & Smith 1998). Here, typical errors are assumed to be about 0.1 to 0.2 dex for both dependent and independent variables.

For the desired relation Y versus X , the fit is described by

$$Y = y_0 + mX. \quad (5)$$

Initially, two linear least-squares fits are obtained : $Y = b_0 + b_1 X$ and $X = a_0 + a_1 Y$. The desired

slope, m , is obtained from the geometric mean of the slopes from the two linear least-squares fits

$$m = \left(\frac{b_1}{a_1} \right)^{1/2}. \quad (6)$$

The desired intercept, y_0 , is given by

$$y_0 = \langle Y \rangle - m \langle X \rangle, \quad (7)$$

where $\langle X \rangle$ and $\langle Y \rangle$ are the averages of X and Y values, respectively. For a given fit, all points are equally weighted.

7.2. Oxygen Abundance versus Luminosity

The metallicity–luminosity diagram has long been considered to be representative of a metallicity–mass relationship for dIs. Skillman, Kennicutt, & Hodge (1989) and Richer & McCall (1995) showed that oxygen abundances in dIs increase with increasing galaxy luminosity in B . Hidalgo-Gámez & Olofsson (1998) claimed from their sample of dIs that this relationship is weaker than previously thought, but low signal-to-noise in their $[\text{O III}]\lambda 4363$ measurements could account for their lack of an observed relation (Pilyugin 2001). Melbourne & Salzer (2002) obtained a metallicity–luminosity correlation for a sample of emission line objects from their KPNO International Spectroscopic Survey. However, their sample included objects at higher luminosities ($M_B \simeq -22$), which may exhibit abundance gradients. Only a small minority of their objects were detected at $[\text{O III}]\lambda 4363$ and other estimates using empirical or bright-line methods (e.g., McGaugh 1991; Pilyugin 2000) were required to derive the remaining oxygen abundances.

Based upon the data presented here, the fitting method described in § 7.1 was applied to obtain a revised fit to the metallicity–luminosity relation. A good correlation is seen in a plot of oxygen abundance against luminosity for the sample of field dIs as shown in Figure 3. The relation for the sample of field dIs is

$$12 + \log (\text{O/H}) = (5.59 \pm 0.54) + (-0.153 \pm 0.025) M_B \quad (8)$$

and the root-mean-square (rms) in $\log(\text{O/H})$ is $\sigma = 0.175$ dex. This fit is shown as a solid line in Figure 3. Equation (8) is consistent with the relation determined by Richer & McCall (1995) for dwarfs brighter than $M_B = -15$. Combining newly acquired data with updates to distances and abundances to other dwarfs has not significantly altered this relation, although the scatter at low luminosities has been reduced (compare with Figure 4, Richer & McCall 1995). Equation (8) will be adopted as the metallicity–luminosity relation for the sample of field dIs.

7.3. Gas, Stellar, and Baryonic Masses

The fraction of baryons in gaseous form is a fundamental quantity, because it determines the metallicity within the “closed box” model of chemical evolution. Dynamical masses have been used in the past to gauge the gas fraction (e.g., Lequeux et al. 1979; Matteucci & Chiosi 1983; Pagel 1986). However, a difficulty with the dynamical mass is that it may be dominated by non-baryonic dark matter, which does not participate in nucleosynthesis. Moreover, dynamical masses are notoriously difficult to measure in dIs, because random or turbulent motions can dominate over ordered or rotational motions, especially at low luminosities (see, e.g., Lo, Sargent, & Young 1993). Instead, it is more prudent to evaluate the gas fraction by estimating masses for the luminous components.

The gas in dIs is the raw material out of which stars and metals are formed and consists mostly of hydrogen and helium. The largest constituent of gas in dIs is assumed to be neutral atomic hydrogen. The composition of gas in molecular form within dIs remains mostly an unknown quantity (see, e.g., Young & Scoville 1991; Hunter & Sage 1993; Israel, Tacconi, & Baas 1995). Although CO is used to trace the molecular hydrogen content in galaxies, the conversion from CO to H₂ masses is uncertain, because there is much debate about the “universality” of the conversion factor. Fortunately, molecular gas is not expected to contribute greatly to the total gas mass in dwarf galaxies, owing to low metallicities and low dust-to-gas ratios (Young & Scoville 1991; Lisenfeld & Ferrara 1998; Vidal et al. 2001). Finally, ionized gas contributes negligibly to the mass (Schombert, McGaugh, & Eder 2001).

The H I mass in solar masses is given by the following equation (Roberts 1975; Roberts & Haynes 1994):

$$M_{HI} = 2.356 \times 10^5 F_{21} D^2, \quad (9)$$

where F_{21} is the 21-cm flux integral in Jy km s⁻¹ and D is the distance in Mpc. Accounting for helium and other metals, the total gas mass in solar masses is given by

$$M_{\text{gas}} = M_{HI}/X, \quad (10)$$

where X is the fraction of the gas mass in the form of hydrogen, adopted to be 0.733.

The mass in stars, M_* , is often computed from the product of the blue luminosity, L_B , with an assumed constant stellar mass-to-light ratio, M_*/L_B . However, this does not account for the possible contamination of the luminosity by bright star-forming regions, which may introduce significant variations in M_*/L_B from galaxy to galaxy. The problem may be particularly severe for dIs, because a star formation event of a given mass would have a proportionately larger effect on the light than it does in a giant spiral galaxy. To account for varying rates of star formation, computing the stellar mass requires a synthesis of stellar populations and it would be ideal to know the flux contributions by old and young stars across a large range of wavelengths. While some recent syntheses of stellar populations within dIs have been founded upon broadband optical and near-infrared colours (e.g., Krüger et al. 1991; Krüger and Alvensleben 1994), all that is widely

available for colours of dIs in the present work is $B - V$. A method is briefly described below which yields an estimate for M_*/L_B tailored to the particular mixture of young and old stars in a dI. Originally developed by M. L. McCall (unpublished) as part of a long-term investigation of the masses of galaxies, this method is described more fully in Lee (2001).

Stellar masses for field dIs were derived by supposing that dIs consist only of a “young” disk component and an “old” disk component. The two-component method is founded upon the assumption that the luminosity of young stars created in a recent burst or bursts of star formation does not overwhelm that from the old stars. Such is the case for dIs, but not for BCDs (Papaderos et al. 1996; Patterson & Thuan 1996). The method is exact if a burst is superimposed upon an old population. A one-component formalism to compute the stellar mass from a “typical” M_*/L_B is not as good as the two-component version, because the stellar mass-to-light ratio may depend on luminosity, and may even vary greatly from galaxy to galaxy at a given luminosity. Lee (2001) has shown that the two-component method gives a tighter correlation between oxygen abundance and the gas mass fraction than the one-component method; see also the discussion at the end of § 7.4.

The mass of stars is given by the sum of the mass in the young and old components

$$\begin{aligned} M_* &= M_{*,\text{yng}} + M_{*,\text{old}} \\ &= \left(\frac{M_*}{L_B} \right)_{\text{yng}} L_{B,\text{yng}} + \left(\frac{M_*}{L_B} \right)_{\text{old}} L_{B,\text{old}}, \end{aligned} \quad (11)$$

where $(M_*/L_B)_{\text{yng}}$ and $(M_*/L_B)_{\text{old}}$ represent the stellar mass-to-light ratios for the young and old components, respectively, and $L_{B,\text{yng}}$ and $L_{B,\text{old}}$ represent the luminosity contributions in B from the young and old components, respectively. The luminosity contributions in B from the young and old components are written as

$$L_{B,\text{yng}} = (1 - f_{\text{old}}) L_B, \quad (12)$$

$$L_{B,\text{old}} = f_{\text{old}} L_B. \quad (13)$$

The fraction of light in B contributed by old stars, f_{old} , is given by

$$f_{\text{old}} = \frac{10^{-0.4(c_{\text{yng}} - c_d)} - 1}{10^{-0.4(c_{\text{yng}} - c_{\text{old}})} - 1}, \quad (14)$$

where c_{yng} , c_{old} , and c_d are, respectively, the $B - V$ colours of the young stars, the old stars, and the entire dI.

The young stellar component is presumed to have properties similar to that of I Zw 18, whose light is known to be dominated by young stars with ages less than 10 Myr old. The intrinsic $B - V$ colour assigned to the young stellar population,

$$c_{\text{yng}} = (B - V)_{\text{yng}}^0 = -0.03 \text{ mag}, \quad (15)$$

is that observed for young dwarf stars ($M_V \lesssim +4$) in the solar neighbourhood (Bahcall & Soneira 1984; van der Kruit 1986) and is consistent with the colour observed for I Zw 18 (Legrand et al.

2000). The mass-to-light ratio in B for young stars is

$$(M_*/L_B)_{\text{yng}} = 0.153 M_\odot/L_{B,\odot}. \quad (16)$$

This mass-to-light ratio comes from models of the distribution of young massive main-sequence stars ($M_V \leq +4.2$) perpendicular to the Milky Way disk, which employ local measures of the luminosity function and mass-luminosity relation (Bahcall 1984; Bahcall & Soneira 1984). The mass-to-light ratio for young stars is taken to be constant, because the initial mass function is found not to vary significantly from galaxy to galaxy (e.g., Massey, Johnson, & DeGioia-Eastwood 1995; Massey et al. 1995; Holtzman et al. 1997). The precise value is not of critical importance, because the mass in typical dwarf galaxies is dominated by old stars and gas.

The “old” component is assumed to consist of old stars and whatever baryonic dark matter is disk-like in its distribution. The intrinsic $B - V$ colour assigned to the old stellar population is given by

$$\begin{aligned} c_{\text{old}} &= (B - V)_{\text{old}}^0 \\ &= (-0.0423 \pm 0.0031) [M_{B,\text{old}} + 1.0454 \langle \mu_{B,\text{eff}}^0 \rangle_{\text{old}}] + (1.177 \pm 0.019), \end{aligned} \quad (17)$$

where $M_{B,\text{old}}$ is the absolute magnitude in B of the old disk, and $\langle \mu_{B,\text{eff}}^0 \rangle_{\text{old}}$ is an estimate for the dust-free mean surface brightness in B of the old disk that would be observed within a circular aperture with radius equal to the effective radius of the disk, if the disk were an oblate spheroid seen face-on. The colour is estimated by assuming that the relationship between $B - V$, luminosity, and surface brightness in old stars is similar to that observed for the ensemble of old stars in disk-like or exponential systems (e.g., dSphs) where star formation has stopped or is occurring at a very low rate and for the old disk of the Milky Way. Dwarf elliptical galaxies in the Local Group and in the Fornax cluster are used to set the relationship; dwarfs as faint as $M_B \approx -9$ set the low-luminosity end of the range. The disks of the Virgo dwarf galaxy VCC 1448, the low surface brightness spiral galaxy Malin 1, and the Milky Way are used to constrain colours at extremes of luminosity and surface brightness. Because the colour of the old population is related to both luminosity and surface brightness, the fraction of light from the old component (Equation 14) must be determined through an iterative process. Based upon what is observed for old stars in elliptical galaxies, the stellar mass-to-light ratio of the old stars is assumed to vary as a power law in luminosity of the old component and is given by

$$\left(\frac{M_*}{L_B} \right)_{\text{old}} = \left(\frac{M_*}{L_B} \right)_{\text{old MW dsk}} \left(\frac{L_{B,\text{old}}}{L_{B,\text{old MW dsk}}} \right)^{\gamma_d}, \quad (18)$$

where $(\frac{M_*}{L_B})_{\text{old MW dsk}}$ and $L_{B,\text{old MW dsk}}$ are, respectively, the mass-to-light ratio and luminosity in B of the old component of the Milky Way disk. The mass-to-light ratio for the old component of the disk of the Milky Way is obtained from the dispersion in vertical motions of disk matter in proximity to the solar neighbourhood. The power law exponent is judged from the relationship between the stellar mass-to-light ratio and luminosity observed for the old disks of spirals and

dwarfs in the Virgo Cluster and is found to be

$$\gamma_d = 0.175 \quad (19)$$

(McCall, private communication). The zero point in Equation (18) is set by the mass-to-light ratio for the old disk of the Milky Way, as judged from the stellar kinematics perpendicular to the Galactic plane (Gould 1990). The derived stellar mass-to-light ratio and the luminosity of the old Milky Way disk, respectively, are given by

$$(M_*/L_B)_{\text{old MW disk}} = 3.11 M_\odot/L_{B,\odot} \quad (20)$$

and

$$L_{B,\text{old MW disk}} = 1.0 \times 10^{10} L_{B,\odot} \quad (21)$$

(McCall, private communication; see also Lee 2001). Combining Equations (11) through (21), the total mass of stars is

$$\begin{aligned} M_* &= M_{*,\text{yng}} + M_{*,\text{old}} \\ &= 0.153 (1 - f_{\text{old}}) L_B + 3.11 \frac{(f_{\text{old}} L_B)^{1.175}}{(1.0 \times 10^{10})^{0.175}}. \end{aligned} \quad (22)$$

Figure 4 shows a plot of the stellar mass-to-light ratio in B versus absolute magnitude in B for field dIs. Two-component stellar mass-to-light ratios in B for the sample of field dIs range between 0.4 and 1.3, with most clustered around unity. There is no strong evidence for a correlation of M_*/L_B with M_B .

Stellar mass-to-light ratios computed with the two-component method agree with predictions of full-scale population syntheses (Bruzual & Charlot 1993, 1996) for systems between 10 and 20 Gyr old which have formed stars at a constant rate (specifically, for a Salpeter stellar initial mass function with mass limits between $0.1 M_\odot$ and $125 M_\odot$, and a metallicity equal to one-fifth solar). Assigning $M_B = -16$ to a dwarf, which is typical of the range for this sample of dIs, the Bruzual & Charlot models produce a dI with $B - V = 0.405$ and $M_*/L_B = 0.757$ at an age of 10 Gyr. For a fiducial dI with $M_B = -16$ and $B - V = 0.405$, the two-component method yields $M_*/L_B = 0.748$, which is in good agreement.

The gas fraction is given by

$$\mu = \frac{M_{\text{gas}}}{M_{\text{bary}}} = \frac{M_{\text{gas}}}{M_{\text{gas}} + M_*}, \quad (23)$$

where the total mass in baryons, M_{bary} , is taken to be the mass of gas and stars. The gas fraction is a distance-independent quantity, because the gas mass and stellar mass are both derived from electromagnetic fluxes. Derived gas masses, stellar masses, stellar mass-to-light ratios, and gas fractions for the sample of field dIs are listed in Table 20.

7.4. Oxygen Abundance versus Gas Fraction

The “closed box” model serves as a useful guide to understanding the chemical evolution of galaxies (Searle & Sargent 1972; Pagel & Patchett 1975; Audouze & Tinsley 1976; Tinsley 1980; Pagel & Edmunds 1981; Edmunds 1990; Köppen 1993; Pagel 1997). Rate equations lead to the following relation between the fraction of the gas mass in the form of a primary product of nucleosynthesis, Z (i.e., the metal abundance), and the fraction of baryonic mass in gaseous form, μ , for a system which evolves in isolation (i.e., neither gaining nor losing mass):

$$Z = y \ln(1/\mu). \quad (24)$$

The constant y is called the yield, which is the ratio of the mass of newly formed metals to the mass of gas permanently locked into stars. Additional premises for the model include an invariant stellar initial mass function (e.g., Massey, Johnson, & DeGioia-Eastwood 1995; Massey et al. 1995; Holtzman et al. 1997; Larson 1999) and instantaneous recycling, which is valid for oxygen produced mainly in massive stars and returned to the interstellar medium when these short-lived stars explode as Type II supernovae (e.g., Burrows 2000).

The metal abundance is best expressed as an elemental abundance in logarithmic form. For oxygen, Equation (24) is rewritten as

$$\log Z_O = \log y_O + \log \ln(1/\mu), \quad (25)$$

where Z_O is the fraction of the gas mass in the form of oxygen. The oxygen abundance by number is then given by

$$\begin{aligned} 12 + \log [N(O)/N(H)] &= 12 + \log(O/H) \\ &= 12 + \log(2.303 y_O / 11.728) + \log \log(1/\mu), \end{aligned} \quad (26)$$

where the numerical factor 2.303 comes from the conversion from a natural logarithm to a logarithm of base ten and the numerical factor 11.728 comes from the conversion from an oxygen abundance by mass to an oxygen abundance by number, assuming that the fraction of gas in the form of hydrogen is $X = 0.733$ (solar value). In a plot of oxygen abundance, $12+\log(O/H)$, against inverse gas mass fraction, conveyed by $\log \log(1/\mu)$, the closed box model predicts a slope of unity. The oxygen yield, y_O , can be derived from the intercept of the plot.

A plot of oxygen abundance against inverse gas mass fraction for field dIs is shown in Figure 5, where an excellent correlation is seen. A fit to all field dIs gives

$$12 + \log(O/H) = (8.63 \pm 0.40) + (1.02 \pm 0.21) \log \log(1/\mu). \quad (27)$$

The rms in $\log(O/H)$ is $\sigma = 0.183$ dex.

IC 1613 appears to have an anomalously small gas mass fraction ($\log \log(1/\mu) \simeq -0.5$) and/or a small abundance ($12+\log(O/H) \simeq 7.7$). The H I mass is unlikely to be problematic,

because the most recent 21-cm flux measurement obtained by Hoffman et al. (1996) has been employed. The measurement of the oxygen abundance may be problematic, however, because the most recent spectroscopic observations are over two decades old (Talent 1980). Another problem may be the reported $B - V$ colour. If it appears too red for its luminosity, the mass judged for the underlying old stellar population would be an overestimate, and, in turn, the gas fraction would be an underestimate.

Excluding IC 1613, the fit is

$$12 + \log(\text{O/H}) = (8.64 \pm 0.40) + (1.01 \pm 0.17) \log \log(1/\mu). \quad (28)$$

The rms in $\log(\text{O/H})$ is reduced to $\sigma = 0.162$ dex, which is lower than the rms in $\log(\text{O/H})$ determined for the fit to the oxygen abundance versus luminosity relationship (Figure 3; Equation 8). Equation (28) is taken as the “best fit” and is shown as a solid line in Figure 5. The fitted slope is consistent with the prediction of the closed box model in Equation (26).

Comparing the intercept in Equation (28) with Equation (26), the effective oxygen yield by mass, y_{O} , is

$$y_{\text{O}} = 2.22 \times 10^{-3}. \quad (29)$$

This result is consistent with that obtained from a fit to a mix of gas-rich dwarf galaxies compiled by Pagel (1986). If $Z_{\odot, \text{O}} = 0.02 \times 0.45 = 0.009$, the present result for the oxygen yield is one-quarter of the value for the solar neighbourhood⁸.

We constructed additional models of chemical evolution by extending the closed box model by accounting for flows; see recent work by, e.g., Edmunds (1990); Pagel (1997); Richer, McCall, & Stasińska (1998, 2001). A full description of the latter will be given by McCall, Richer, & Stasińska (in preparation). In short, the flow rate is a multiple of the star formation rate (i.e., linear flows, constant with time; see e.g., Matteucci & Chiosi 1983; Edmunds 1990; Köppen 1993). In the analytical formulation, the explicit time dependence cancels out. The metallicity of the flowing gas is either zero for inflow, or equal to the metallicity of the interstellar medium for outflow. The adopted yield is the same derived above in Equation (29).

The predicted relations from models with gas flows are shown in Figure 5. Outflow and inflow models are indicated as dotted and dashed curves, respectively. In each set of models, the flow rate increases from the top curve to the bottom curve. For outflow models, the slopes of the model curves decrease as the flow rates increase. For inflow rates higher than the star formation rate, the shape of the curve deviates from a straight line and turns over at low gas fractions. Nonzero flow rates exceeding the star formation rate are allowed, but not forced. The simplest explanation consistent with the data is that the flow rates are zero (i.e., dIs as closed systems), although

⁸The solar value of the oxygen abundance of $12 + \log(\text{O/H}) = 8.87$ is adopted for the present work (Grevesse, Noels, & Sauval 1996). However, recent results (e.g., Allende Prieto, Lambert, & Asplund 2001) have shown that the solar value may in fact be smaller by ≈ 0.2 dex.

the observations admit the possibility that there were moderate flows. It would be interesting to augment the number of metal-poor dwarf irregular galaxies to help “anchor” the slope at high gas fractions and to augment the number of dwarf galaxies with $[\text{O III}]\lambda 4363$ abundances at lower gas fractions to see whether the trend “turns over” towards nonzero flows.

The value of the metallicity-gas fraction diagram in studying chemical evolution is that statements about chemical evolution, especially the importance of gas flows, can be made without knowledge of the detailed history of star formation. On its own, the metallicity-luminosity diagram says nothing about flows. It is simply evidence of a relationship between metallicity and a parameter that depends upon luminosity. For closed box evolution, that parameter could be (a) the average star formation rate, if all dIs have been forming stars for the same length of time, or (b) the star formation time scale, if all dIs have been forming stars at the same average rate, or (c) some combination of the two for more complicated star formation scenarios. Recent studies (e.g., Gallagher, Hunter, & Tutukov 1984; van Zee 2001) have shown that stars in dwarf irregulars have formed steadily but slowly. Since the metallicity-gas fraction diagram suggests that field dwarfs have not suffered from extreme flows of gas, then one would conclude that the metallicity-luminosity relation is a consequence of variations in the time scale for star formation.

Values of μ depend on M_* , which in turn comes from the two-component algorithm of population synthesis. It is worthwhile examining the ingredients of the algorithm to determine the robustness of the conclusion that field dIs have evolved as closed systems. Four variants are considered: (1) the mass-to-light ratio for old stars is fixed at the value for the old disk of the Milky Way (see Equation 20), (2) the mass-to-light ratio for old stars is fixed at the mean value (1.50) for all dIs in the sample, (3) the mass-to-light ratio for old stars varies with the luminosity of the old component as a power law, and the $B - V$ colour for old stars is fixed at the mean value (0.74) for all dIs in the sample, and (4) the mass-to-light ratio for *all* stars is fixed at unity, motivated by the Bruzual & Charlot (1996) models and the absence of any trend in $B - V$ colour with B luminosity (Lee 2001). In each case, M_* and μ were computed, and a best fit to $\log(\text{O/H})$ vs. $\log \log (1/\mu)$ was determined using the geometric mean functional relationship.

Table 21 lists the effects of the presumptions on the relationship described by Equation (26). The exclusion of the data point corresponding to IC 1613 from all models does not significantly affect the results. All fits have slopes consistent with unity. The smallest dispersion in the relationship between the oxygen abundance and the gas fraction is obtained when the mass-to-light ratio in the old disk component has a power-law dependence on the luminosity of the old disk, as employed in the two-component algorithm. Hence, the conclusion that field dIs have evolved as closed systems does not depend critically upon the details of the population synthesis.

8. Conclusions

The evolution of dwarf irregular galaxies in the field must be understood before it is possible to study how the evolution of dIs in clusters of galaxies has been affected by the denser environment. A suitable control group was constructed from a sample of nearby dIs with $[\text{O III}]\lambda 4363$ measurements and well-measured distances. Distance determinations and oxygen abundance measurements were updated with recently published values. Oxygen abundances for five field dIs were updated using spectroscopy acquired at Steward Observatory and at the Observatorio Astronómico Nacional in México.

Two diagrams were examined as diagnostics for the evolution of dIs. The metallicity–luminosity relationship has been considered as a proxy for the metallicity–mass relationship, at least where stellar mass is concerned. The updated relationship between oxygen abundance and luminosity for the present sample of field dIs is similar to that found by Skillman, Kennicutt, & Hodge (1989) and Richer & McCall (1995). The relationship between metallicity and the gas fraction is a gauge of the progress by which gas is being converted into stars and metals. The gas fraction was judged using the masses of luminous components in the form of stars and gas, which are constituents of the nucleogenetic pool. This is preferable to the past use of dynamical masses that may be dominated by non-baryonic dark matter, which does not participate in nucleosynthesis. A strong correlation between oxygen abundance and the gas fraction, defined as the ratio of gas mass to the total baryonic mass, was found for field dIs. The data are consistent with zero gas flows (i.e., evolution as isolated systems), although the observations do admit the possibility of modest flows. The oxygen yield is about one-quarter of the value found in the solar neighbourhood.

It is now possible to use the diagnostic diagrams to study the evolution of dwarfs in clusters of galaxies by looking for an offset between a sample of cluster dwarfs and a control sample of dwarfs in the field. The present results are applied to a study of dwarf irregulars in the Virgo Cluster, which is the subject of Paper II.

The work presented here was part of the dissertation completed by HL at York University in Toronto, Canada. HL is grateful to Marshall McCall for guidance, supervision, and financial support. HL also thanks Dan Zucker, Michael Richer, and the anonymous referee for constructive comments which improved the presentation of this paper. MLM acknowledges the Natural Sciences and Engineering Research Council of Canada for its continuing support. MLM, RLK, and CCS thank the staff at the Observatorio Astronómico Nacional at San Pedro Mártir and the Steward Observatory for their help with observations. Some data were accessed as Guest User, Canadian Astronomy Data Center, which is operated by the Dominion Astrophysical Observatory for the National Research Council of Canada's Herzberg Institute of Astrophysics. This research has made use of the NASA/IPAC Extragalactic Database (NED), which is operated by the Jet Propulsion Laboratory, California Institute of Technology, under contract with the National Aeronautics and Space Administration.

REFERENCES

Aaronson, M., 1986, in *Star Forming Dwarf Galaxies and Related Objects*, ed. D. Kunth, T. X. Thuan, & J. T. T. Van, Paris: Editions Frontières, 125

Aaronson, M., Cohen, J. G., Mould, J., & Malkan, M. 1978, *ApJ*, 223, 824

Allende Prieto, C., Lambert, D. L., & Asplund, M. 2001, *ApJ*, 556, L63

Aparicio, A., Tikhonov, N., & Karachentsev, I. 2000, *AJ*, 119, 177

Audouze, J., & Tinsley, B. M. 1976, *ARA&A*, 14, 43

Bahcall, J. N. 1984, *ApJ*, 287, 926

Bahcall, J. N., & Soneira, R. M. 1984, *ApJS*, 55, 67

Bender, R., Burstein, D., & Faber, S. M. 1992, *ApJ*, 399, 462

Bhatia, A. K., & Kastner, S. O. 1995, *ApJS*, 96, 325

Binggeli, B. 1994, in *Dwarf Galaxies (ESO/OHP Conference and Workshop Proceedings 49)*, ed. G. Meylan and P. Prugniel, Garching bei München: European Southern Observatory, 13

Binggeli, B., Sandage, A., & Tammann, G. A. 1985, *AJ*, 90, 1681

Binggeli, B., Sandage, A., & Tarenghi, M. 1984, *AJ*, 89, 64

Bothun, G. D., Eriksen, J., & Schombert, J. M. 1994, *AJ*, 108, 913

Bothun, G. D., Mould, J. R., Caldwell, N., & MacGillivray, H. T. 1986, *AJ*, 92, 1007

Bruzual, G., & Charlot, S. 1993, *ApJ*, 405, 538

Bruzual, G., & Charlot, S. 1996, Vol. 7, *Astrophysics on Disc (AAS CD-ROM Series)*, Washington: American Astron. Society (see § 6.4, Leitherer et al. 1996)

Burrows, A. 2000, *Nature*, 403, 727

Buta, R. J., & McCall, M. L. 1999, *ApJS*, 124, 33

Calzetti, D. 2001, *PASP*, 113, 1449

Cardelli, J. A., Clayton, G. C., & Mathis, J. S. 1989, *ApJ*, 345, 245

Cioni, M.-R. L., van der Marel, R. P., Loup, C., & Habing, H. J. 2000, *A&A*, 359, 601

Cole, A. A., Tolstoy, E., Gallagher, J. S., Hoessel, J. G., Mould, J. R., Holtzman, J. A., Saha, A., Ballester, G. E., Burrows, C. J., Clarke, J. T., Crisp, D., Griffiths, R. E., Grillmair, C. J., Hester, J. J., Krist, J. E., Meadows, J., Scowen, P. A., Stapelfeldt, K. R., Trauger, J. T., Watson, A. M., & Westphal, J. R. 1999, *AJ*, 118, 1657

Côté, P., Marzke, R. O., West, M. J., & Minniti, D. 2000, *ApJ*, 533, 869

Davies, J. I., & Phillipps, S. 1988, *MNRAS*, 233, 533

Davies, J. I., & Phillipps, S. 1989, *Astr. Sp. Sci.* 157, 291

Dekel, A., & Silk, J. 1986, *ApJ*, 303, 39

DellaCeca, R., Griffiths, R. E., & Heckman, T. M. 1997, *ApJ*, 485, 581

De Robertis, M. M., Dufour, R. J., & Hunt, R. W. 1987, *JRASC*, 81, 195

Devost, D., Roy, J.-R., & Drissen, L. 1997, *ApJ*, 482, 765

Dinerstein, H. L. 1990, in *The Interstellar Medium in Galaxies*, ed. H. A. Thronson & J. M. Shull, Dordrecht: Kluwer Academic Publishers, 257

Dohm-Palmer, R. C., Skillman, E. D., Gallagher, J. S., Tolstoy, E., Mateo, M., Dufour, R. J., Saha, A., Hoessel, J. G., & Chiosi, C. 1998, *AJ*, 116, 1227

Draper, N. R., & Smith, H., 1998, *Applied Regression Analysis*, New York: Wiley, 89

Driver, S. P., & Cross, N. 2000, in *Mapping the Hidden Universe (A.S.P. Conf. Ser. 218)*, ed. R. C. Kraan-Korteweg, P. A. Henning, & H. Andernach, San Francisco: Astron. Soc. of the Pacific, 309

Edmunds, M. G. 1990, *MNRAS*, 246, 678

Faber, S. M., & Lin, D. N. C. 1983, *ApJ*, 266, L17

Ferguson, H. C. 1989, *Astrophys. Sp. Sci.* 157, 227

Ferguson, H. C., & Binggeli, B. 1994, *A&A Rev.* 6, 67

Ferrara, A., & Tolstoy, E. 2000, *MNRAS*, 313, 291

Gallagher, J. S., & Hunter, D. A. 1984, *ARA&A*, 22, 37

Gallagher, J. S., Hunter, D. A., & Tutukov, A. V. 1984, *ApJ*, 284, 544

Gallart, C., Aparicio, A., & Vílchez, J. M. 1996, *AJ*, 112, 1928

González-Delgado, R. M., Pérez, E., Tenorio-Tagle, G., Vílchez, J. M., Terlevich, E., Terlevich, R., Telles, E., Rodríguez-Espinosa, J. M., Mas-Hesse, M., García-Vargas, M. L., Díaz, A. I., Cepa, J., & Castañeda, H. 1994, *ApJ*, 437, 239

Gould, A. 1990 *MNRAS*, 244, 25

Grebel, E. K., & Guhathakurta, P. 1999, *ApJ*, 511, L101

Greggio, L., Tosi, M., Clampin, M., De Marchi, G., Leitherer, C., Nota, A., & Sirianni, M. 1998, *ApJ*, 504, 725

Grevesse, N., Noels, A., & Sauval, A. J. 1996, in *Cosmic Abundances: Proceedings of the 6th Annual October Astrophysics Conference*, A.S.P. Conference Series Vol. 99, ed. S. S. Holt & G. Sonneborn, San Francisco: Astron. Soc. of the Pacific, 117

Heckman, T. M., Dahlem, M., Lehnert, M. D., Fabbiano, G., Gilmore, D., & Waller, W. H. 1995, *ApJ*, 448, 98

Hidalgo-Gámez, A. M., & Olofsson, K. 1998, *A&A*, 334, 45

Hodge, P., & Lee, M. G. 1990, *PASP*, 102, 26

Hodge, P., & Miller, B. W. 1995, *AJ*, 451, 176

Hodge, P., Strobel, N. V., & Kennicutt, R. C. 1994, *PASP*, 106, 309

Hoessel, J. G., Saha, A., & Danielson, G. E. 1998, *AJ*, 115, 573

Hoessel, J. G., Saha, A., & Danielson, G. E. 1998, *AJ*, 116, 1679

Hoessel, J. G., Saha, A., Krist, J., & Danielson, G. E. 1994, *AJ*, 108, 645

Hoffman, G. L., Salpeter, E. E., Farhat, B., Roos, T., Williams, H., & Helou, G. 1996, *ApJS*, 105, 269

Holtzman, J. A. et al. 1997, *AJ*, 113, 656

Huchtmeier, W. K., & Richter, O. G. 1986, *A&AS*, 63, 323

Hunter, D. A. 1997, *PASP*, 109, 319

Hunter, D. A. & Gallagher, J. S. 1985, *ApJS*, 58, 533

Hunter, D. A. & Gallagher, J. S. 1986, *PASP*, 98, 5

Hunter, D. A. & Gallagher, J. S. 1989, *Science*, 243, 1557

Hunter, D. A., & Hoffman, L. 1999, *AJ*, 117, 2789

Hunter, D. A., & Sage, L. 1993, *PASP*, 105, 374

Hunter, D. A., Hawley, W. N., & Gallagher, J. S. 1993, *AJ*, 106, 1797

Israel, F. P., Tacconi, L. J., & Baas, F. 1995, *A&A*, 295, 599

Izotov, Y. I., Thuan, T. X., & Lipovetsky, V. A. 1997, *ApJS*, 108, 1

Kingsburgh, R. L., & Barlow, M. J. 1995, *A&A*, 295, 171

Kobulnicky, H. A., & Skillman, E. D. 1996, *ApJ*, 471, 211

Kobulnicky, H. A., & Skillman, E. D. 1997, *ApJ*, 489, 636

Köppen, J. 1993, *Rev. Mod. Astronomy*, 6, 179

Kormendy, J. 1985, *ApJ*, 295, 73

Krawchuk, C., McCall, M. L., Komljenovic, M., Kingsburgh, R., Richer, M., & Stevenson, C. 1997, in *IAU Symposium 180, Planetary Nebulae*, ed. H. J. Habing & H. J. G. L. M. Lamers, Dordrecht: Kluwer, 116

Krüger, H., & Alvensleben, U. F.-v. 1994, *A&A*, 284, 793

Krüger, H., Alvensleben, U. F.-v., Loose, H.-H., & Fricke, K. J. 1991, *A&A*, 242, 343

van der Kruit, P. C. 1986, *A&A*, 157, 230

Larson, R. B. 1999, in *Star Formation 1999*, ed. T. Nakamoto, Nobeyama Radio Observatory, 336

Lee, H., 2001, Ph.D. thesis, York University

Lee, M. G., & Madore, B. F. 1993, *AJ*, 106, 66

Lee, M. G., Freedman, W. L., & Madore, B. F. 1993, *ApJ*, 417, 553

Legrand, F., Kunth, D., Roy, J.-R., Mas-Hesse, J. M., & Walsh, J. R. 2000, *A&A*, 355, 891

Leitherer, C. et al. 1996, *PASP*, 108, 996

Lennon, D. J., & Burke, V. M. 1994, *A&AS*, 103, 273

Lequeux, J., Peimbert, M., Rayo, J. F., Serrano, A., & Torres-Peimbert, S. 1979, *A&A*, 80, 155

Lin, D. N. C., & Faber, S. M. 1983, *ApJ*, 266, L21

Lisenfeld, U., & Ferrara, A. 1998, *ApJ*, 496, 145

Lo, K. Y., Sargent, W. L. W., & Young, K. 1993, *AJ*, 106, 507

Lynds, R., Tolstoy, E., O’Neil, E. J., & Hunter, D. A. 1998, *AJ*, 116, 146

Mac Low, M., & Ferrara, A. 1999, *ApJ*, 513, 142

Madore, B. F., & Freedman, W. L. 1991, *PASP*, 103, 933

Martin, C. 1996, *ApJ*, 465, 680

Marzke, R. O., & Da Costa, L. N. 1997, *AJ*, 113, 185

Masegosa, J., Moles, M., & del Olmo, A. 1991, *A&A*, 249, 505

Massey, P., Johnson, K. E., & DeGioia-Eastwood, D. 1995, *ApJ*, 454, 151

Massey, P., Lang, C. C., DeGioia-Eastwood, K., & Garmany, C. D. 1995, *ApJ*, 438, 188

Mateo, M. 1998, *ARA&A*, 36, 435

Matteucci, F., & Chiosi, C. 1983, *MNRAS*, 123, 121

McCall, M. L., Rybski, P. M., & Shields, G. A. 1985, *ApJS*, 57, 1

McGaugh, S. S. 1991, *ApJ*, 380, 140

McLaughlin, B. M., & Bell, K. L. 1993, *ApJ*, 408, 753

Melbourne, J., & Salzer, J. J. 2002, *AJ*, 123, 2302

Meurer, G. R. 1998, in *Dwarf Galaxies and Cosmology*, ed. T. X. Thuan, C. Balkowski, V. Cayatte, & J. T. Than Van, Paris: Editions Frontières

Miller, B. W. 1996, *AJ*, 112, 991

Miller, B. W., & Hodge, P. 1996, *ApJ*, 458, 467

Minniti, D., & Zijlstra, A. A. 1997, *AJ*, 114, 147

Minniti, D., Zijlstra, A. A., & Alonso, M. V. 1999, *AJ*, 117, 881

Musella, I., Piotto, G., & Capaccioli, M. 1997, *AJ*, 114, 976

Osterbrock, D. E. 1989, *Astrophysics of Gaseous Nebulae and Active Galactic Nuclei*, Mill Valley: University Science Books

Pagel, B. E. J. 1986, *Highlights in Astronomy*, 7, 551

Pagel, B. E. J. 1997, *Nucleosynthesis and the Chemical Evolution of Galaxies*, Cambridge: Cambridge University Press

Pagel, B. E. J., & Edmunds, M. G. 1981, *ARA&A*, 19, 77

Pagel, B. E. J., & Patchett, B. E. 1975, *MNRAS*, 172, 13

Panagia, N. 1999, in *IAU Symposium 190, New Views of the Magellanic Clouds*, ed. Y. H. Chu, N. Suntzeff, J. Hesser, & D. Bohlender, San Francisco: Astron. Soc. of the Pacific, 549

Papaderos, P., Loose, H.-H., Fricke, K. J., & Thuan, T. X. 1996, *A&A*, 314, 59

Patterson, R. J., & Thuan, T. X. 1996, *ApJS*, 107, 103 (erratum: 1998, *ApJS*, 117, 633)

Phillipps, S., Parker, Q. A., Schwartzenberg, J. M., & Jones, J. B. 1998, *ApJ*, 493, L59

Pilyugin, L. S. 2000, *A&A*, 362, 325

Pilyugin, L. S. 2001, *A&A*, 374, 412

Prada, F., & Burkert, A. 2002, *ApJ*, 564, L73

Pradhan, A. K. 1976, *MNRAS*, 177, 31

Puche, D., Westpfahl, D., Brinks, E., & Roy, J.-R. 1992, *AJ*, 103, 1841

Richer, M. G., & McCall, M. L. 1992, *ApJ*, 103, 54

Richer, M. G., & McCall, M. L. 1995, *ApJ*, 445, 642

Richer, M. G., McCall, M. L., & Stasińska, G. 1998, *A&A*, 340, 67

Richer, M. G., McCall, M. L., & Stasińska, G. 2001, in *Focal Points in Latin American Astronomy*, ed. A. Aguilar, & A. Carramiñana, *Revista Mexicana de Astronomía y Astrofísica Serie de Conferencias*, 117

Richer, M. G., Bullejos, A., Borissova, J., McCall, M. L., Lee, H., Kurtev, R., Georgiev, L., Kingsburgh, R. L., Ross, R., & Rosado, M. 2001, *A&A*, 370, 34

Roberts, M. S., 1975, in *Galaxies and the Universe*, ed. A. Sandage, M. Sandage, & J. Kristian, Chicago: University of Chicago Press, 309

Roberts, M. S., & Haynes, M. P. 1994, *ARA&A*, 32, 115

Saha, A., Hoessel, J. G., Krist, J., & Danielson, G. E. 1996, *AJ*, 111, 197

Sakai, S., Madore, B. F., Freedman, W. L. 1996, *ApJ*, 461, 713

Sakai, S., Madore, B. F., Freedman, W. L. 1997, *ApJ*, 480, 589

Sakai, S., Madore, B. F., Freedman, W. L. 1999, *ApJ*, 511, 671

Sakai, S., Zaritsky, D., Kennicutt, R. C. 2000, *AJ*, 119, 1197

Schombert, J., McGaugh, S. S., & Eder, J. A. 2001, *AJ*, 121, 2420

Schulte-Ladbeck, R. E., Crone, M. M., & Hopp, U. 1998, *ApJ*, 493, L23

Searle, L., & Sargent, W. L. W. 1972, *ApJ*, 173, 25

Secker, J., Harris, W. E., & Plummer, J. D. 1997, *PASP*, 109, 1377

Shields, G. A. 1990, *ARA&A*, 28, 525

Skillman, E. D. 1997, Rev. Mex. Astron. Astrof. Serie de Conferencias, 6, 36

Skillman, E. D., Kennicutt, R. C., & Hodge, P. 1989, ApJ, 347, 875.

Smith, G. H. 1985, PASP, 97, 1058

Stil, J. M., & Israel, F. P. 2002, A&A, 392, 473

Storey, P. J., & Hummer, D. G. 1995, MNRAS, 272, 41

Strickland, D. K., Ponman, T. J., & Stevens, I. R. 1997, A&A, 320, 378

Strobel, N. V., Hodge, P., & Kennicutt, R. C. 1991, ApJ, 383, 148

Talent, D. L. 1980, Ph.D. thesis, Rice University

Thuan, T. X. 1985, ApJ, 299, 881

Tinsley, B. 1980, Fund. Cosmic Phys., 5, 287

Tolstoy, E., Saha, A., Hoessel, J. G., & Danielson, G. E. 1995, AJ, 109, 579

Tolstoy, E., Saha, A., Hoessel, J. G., & McQuade, K. 1995, AJ, 110, 1640

Tolstoy, E., Gallagher, J. S., Cole, A. A., Hoessel, J. G., Saha, A., Dohm-Palmer, R. C., Skillman, E. D., Mateo, M., & Hurley-Keller, D. 1998, AJ, 116, 1244

Tully, R. B., Boesgaard, A. M., Dyck, H. M., & Schempp, W. V. 1981, ApJ, 246, 38

Vidal-Madjar, A., et al. 2001, ApJ, 538, L77

Wiese, W. L., Fuhr, J. R., & Deters, T. M. Atomic transition probabilities of carbon, nitrogen, and oxygen : a critical data compilation, American Chemical Society for the National Institute of Standards and Technology (NIST), 1996

Wilson, C. D., Welch, D. L., Reid, I. N., Saha, A., & Hoessel, J. G. 1996, AJ, 111, 1106

Young, J. S., & Scoville, N. Z. 1991, ARA&A, 29, 581

van Zee, L., Haynes, M. P., & Salzer, J. J. 1997, AJ, 114, 2479

van Zee, L. 2001, AJ, 121, 2003

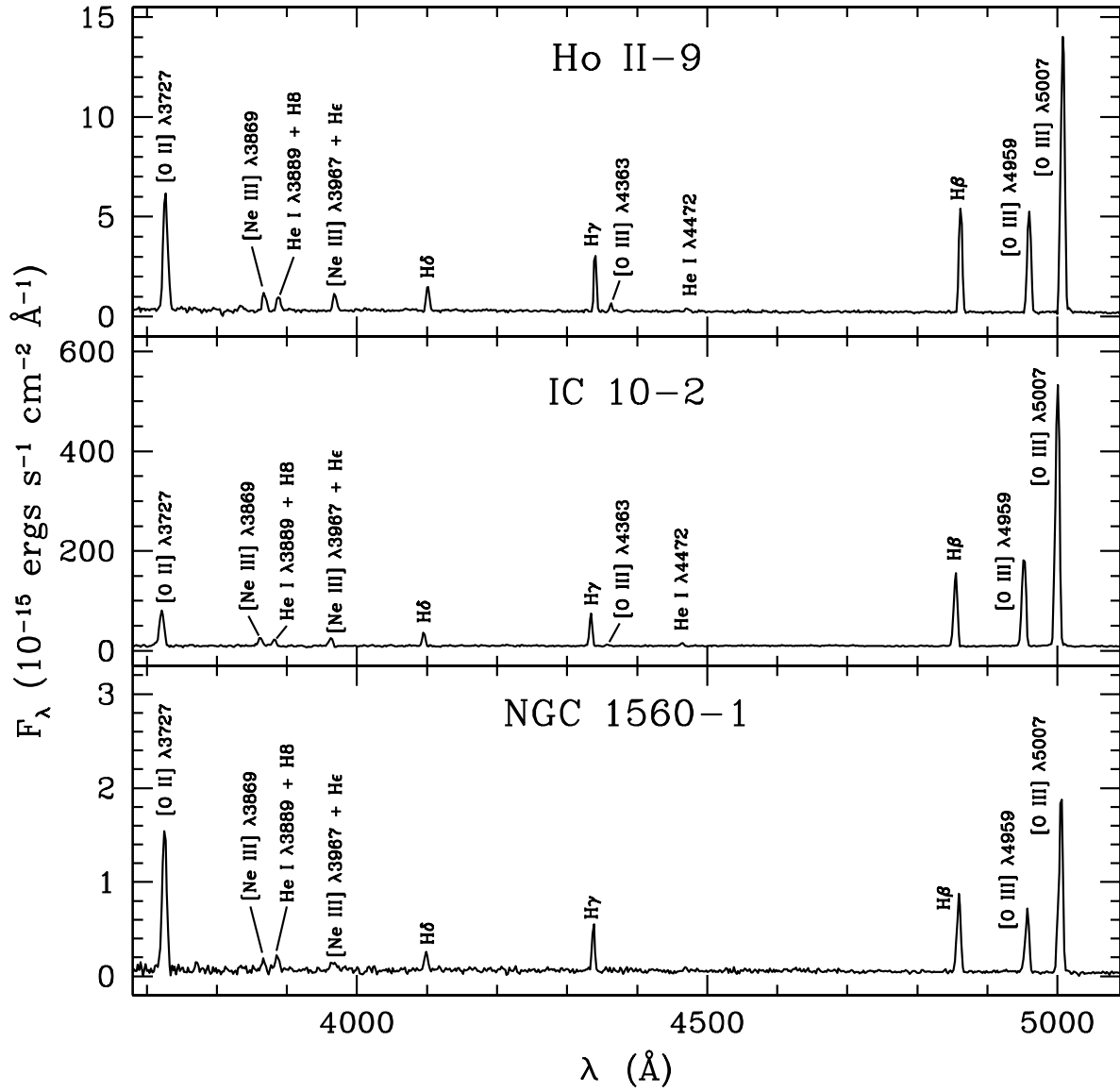


Fig. 1.— Optical emission-line spectra of Holmberg II-9, IC 10-2, and NGC 1560-2 from Steward Observatory. The observed flux per unit wavelength is plotted versus wavelength. Key emission lines are labelled.

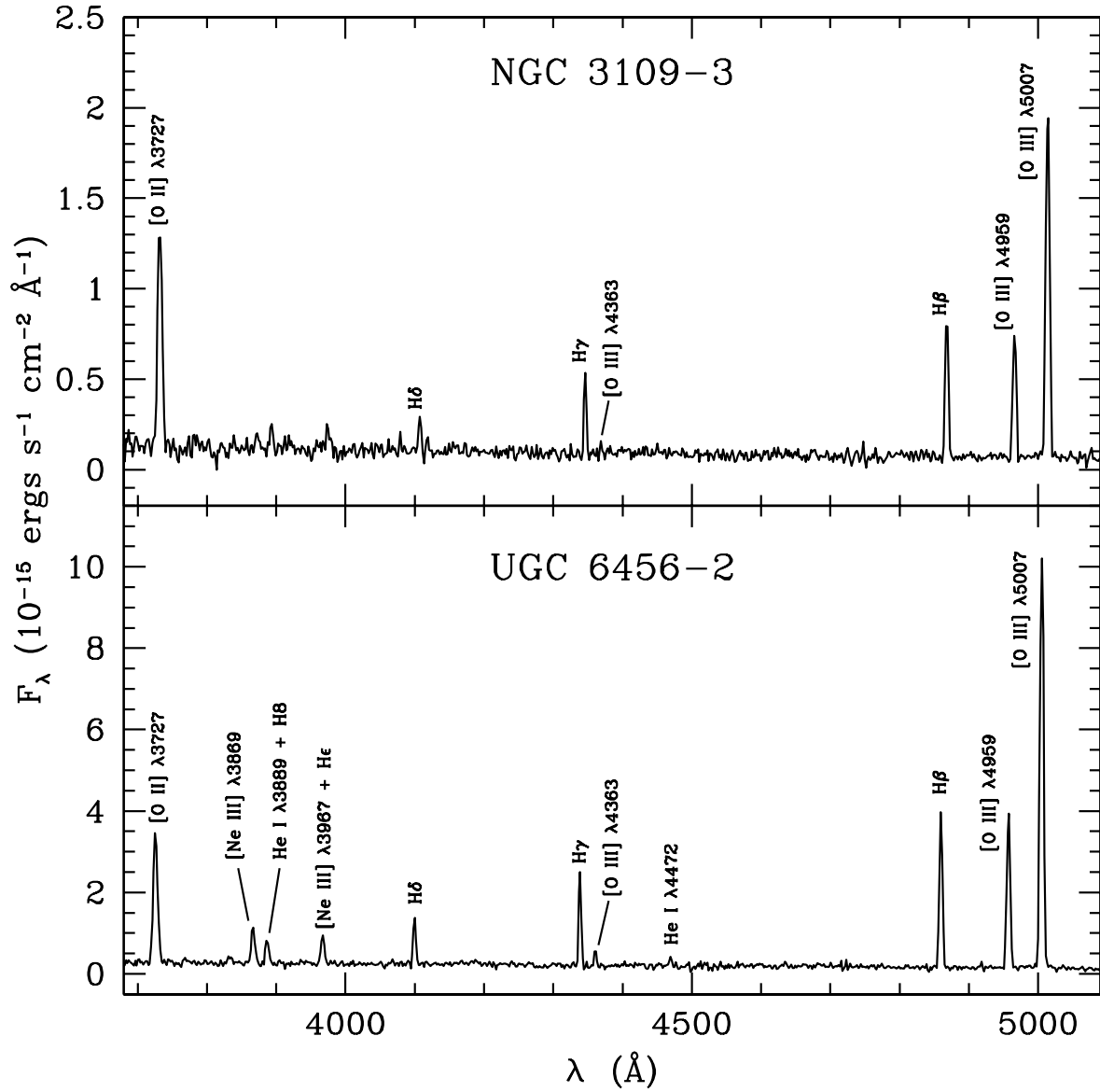


Fig. 2.— Optical emission-line spectra of NGC 3109-3 and UGC 6456-2 from Steward Observatory. The observed flux per unit wavelength is plotted versus wavelength. Key emission lines are labelled.

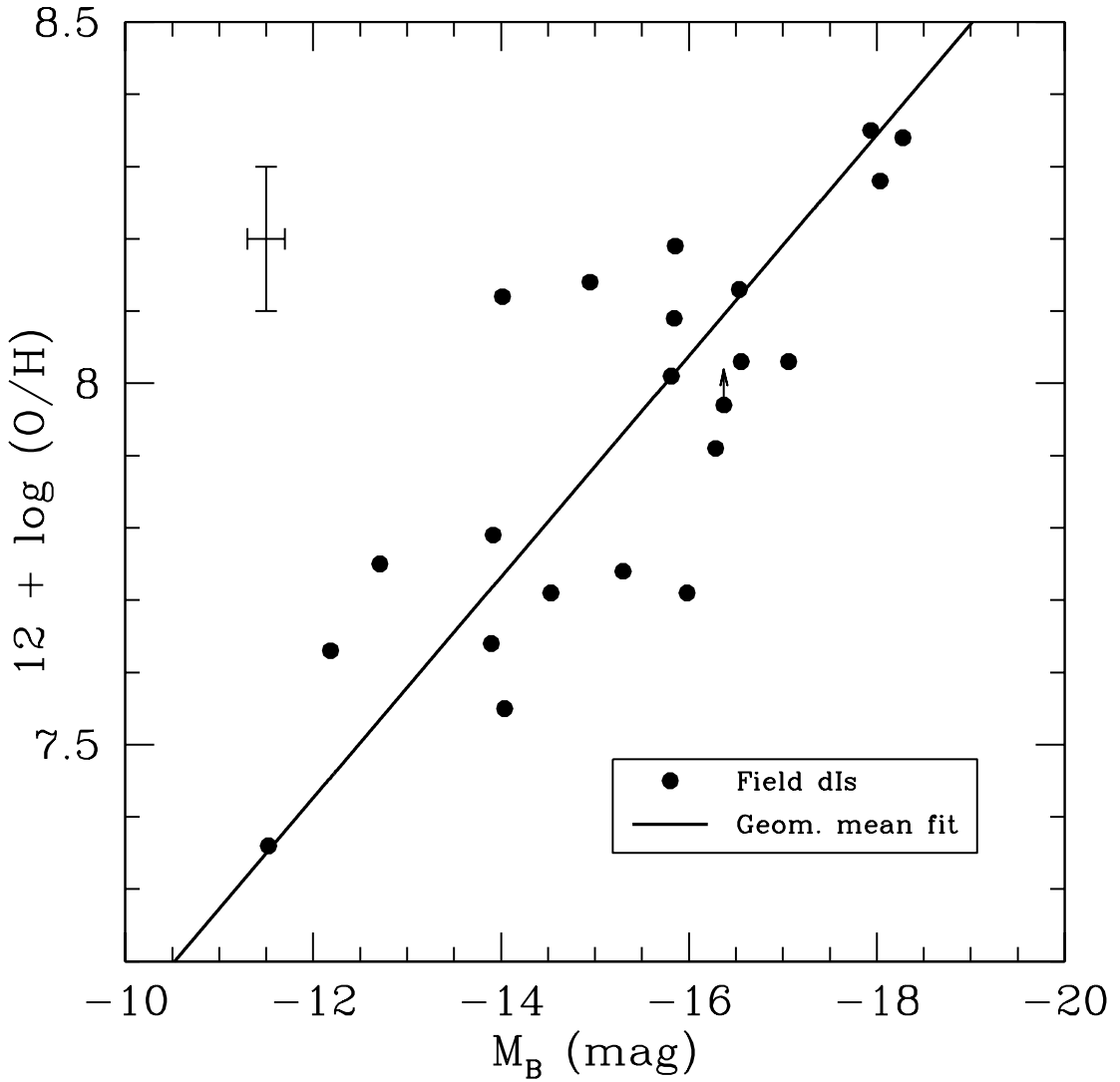


Fig. 3.— Oxygen abundance versus absolute magnitude in B for field dIs. Galaxy luminosity increases to the right. The filled circles mark the field dIs. The arrow indicates a lower limit to the oxygen abundance for NGC 1560. Oxygen abundances for the field dwarfs were determined directly from [O III] $\lambda 4363$ measurements. The solid line is a fit to the field dIs (Equation 8) using the geometric mean functional relation (Draper & Smith 1998). The error bars indicate typical uncertainties in the oxygen abundance and absolute magnitude. The uncertainty is at most 0.1 dex for oxygen abundances which were determined directly from [O III] $\lambda 4363$ measurements. An uncertainty of 0.2 mag in absolute magnitude is typical of what can arise from distance determinations.

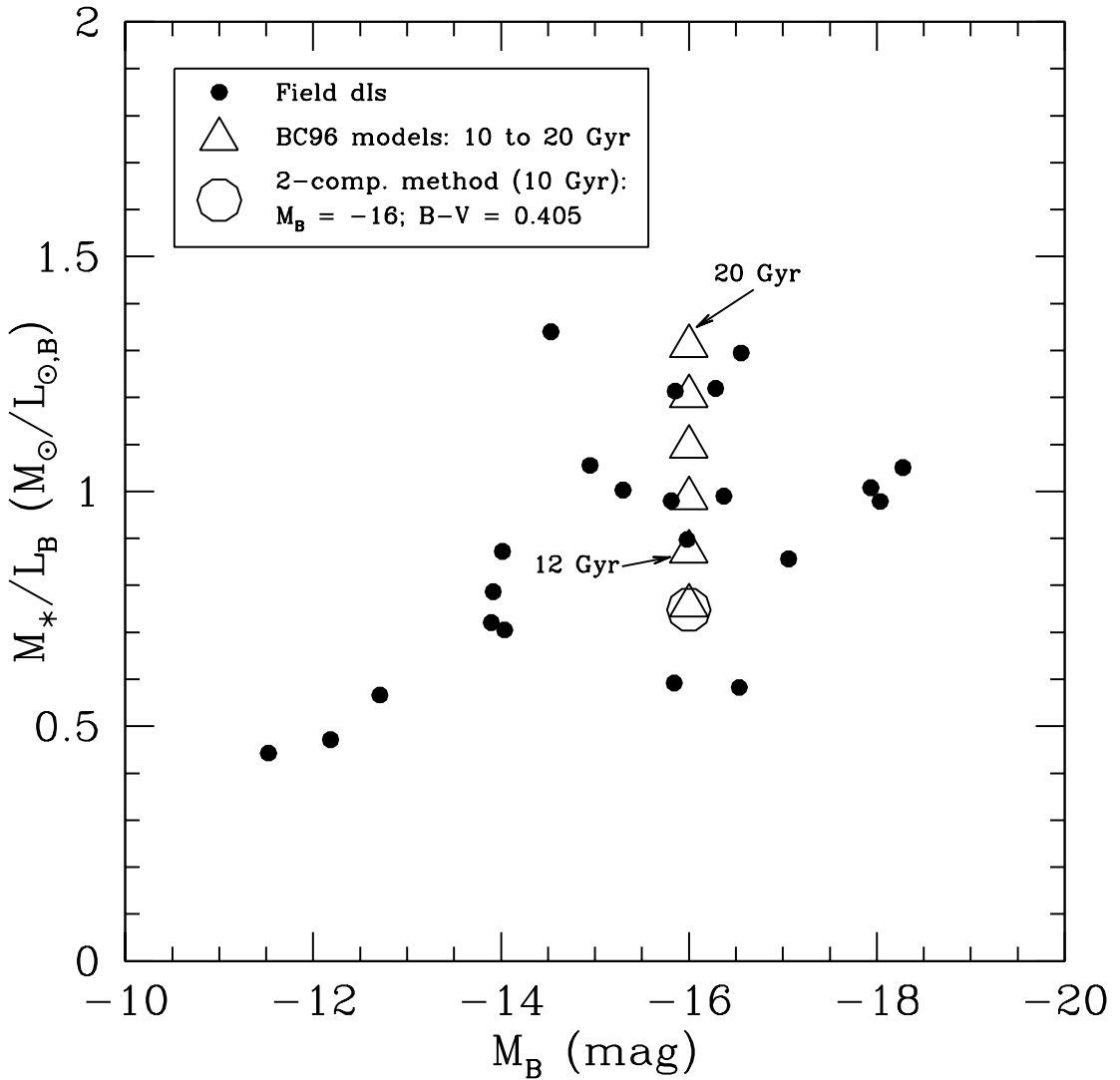


Fig. 4.— Stellar mass-to-light ratio versus absolute magnitude in B for field dIs. Filled circles mark the field dIs. For ages between 10 and 20 Gyr in increments of 2 Gyr, open triangles show the locations of a fiducial $M_B = -16$ dwarf galaxy, whose properties are determined from the evolutionary synthesis code of Bruzual & Charlot (1996, BC96). The open circle shows the position of a 10 Gyr old dI with $M_B = -16$ and $B - V = 0.405$ for which values of M_* are obtained from the two-component method.

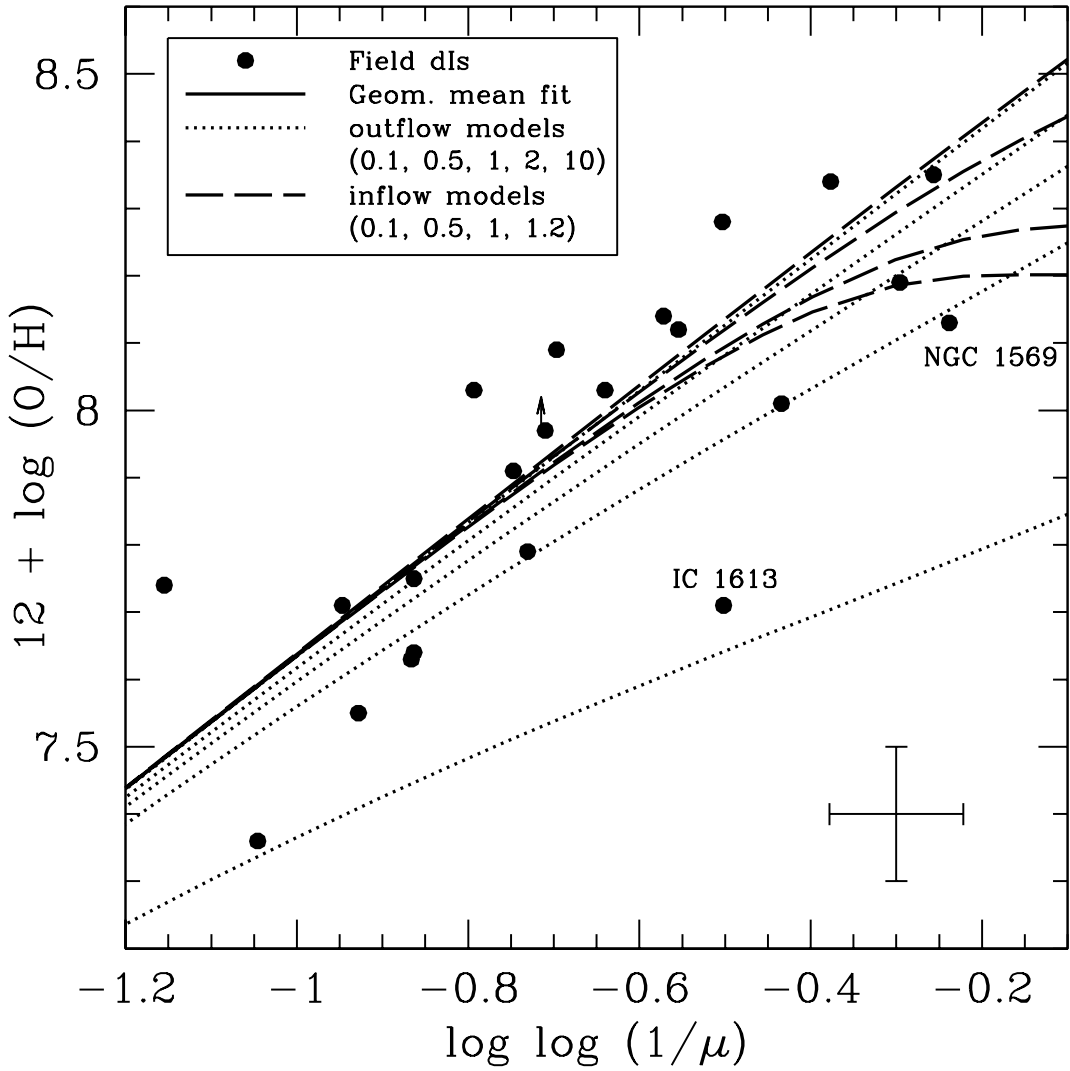


Fig. 5.— Oxygen abundance versus fraction of baryons in the form of gas for field dIIs. The abundance increases upwards and gas fraction decreases to the right. Filled circles mark the field dIIs. Data points representing the dwarfs IC 1613 and NGC 1569 are labelled. The upward arrow indicates a lower limit to the oxygen abundance for NGC 1560. The solid line is a geometric mean fit to the field dIIs (Equation 28) consistent with the closed box model. Dotted and dashed curves indicate different outflow and inflow models, respectively. The flow rate, which is taken to be proportional to the star formation rate, increases from the top curve to the bottom curve in each set of inflow and outflow models. The error bars indicate typical uncertainties of 0.1 dex in oxygen abundance and 0.1 dex in $\log \log (1/\mu)$. The latter uncertainty is derived from an estimated 0.05 mag uncertainty in $B - V$, which affects the derivation of M_* , and an estimated 20% uncertainty in H I gas mass (Huchtmeier & Richter 1986).

Table 1. The sample of dwarf irregular galaxies in the field.

Name	M_B (mag)	$(m - M)^0$ (mag)	$(B - V)_T^0$ (mag)	F_{21} (Jy km s $^{-1}$)	12+log(O/H) (dex)
(1)	(2)	(3)	(4)	(5)	(6)
DDO 187	−12.72	27.10	0.38	14.2	7.69 ± 0.09
GR 8	−12.19	26.83	0.31	8.6	7.63 ± 0.14
Holmberg II	−15.98	27.50	0.42	359.7	7.71 ± 0.13
IC 10 ^a	−15.85	24.47	0.69	950.4	8.19 ± 0.14
IC 1613	−14.53	24.38	0.67	698	7.71 ± 0.15
IC 2574	−17.06	27.86	0.35	442.5	8.09 ± 0.07
IC 4662	−15.84	27.32	0.35	125.2	8.09 ± 0.04
Leo A	−11.53	24.45	0.32	68.4	7.36 ± 0.06
LMC	−17.94	18.58	0.45	1.044×10^6	8.35 ± 0.06
NGC 55	−18.28	25.94	0.46	2679	8.34 ± 0.10
NGC 1560	−16.37	27.07	0.49	443	> 7.97
NGC 1569 ^b	−16.54	26.39	0.35	116	8.19 ± 0.06
NGC 2366	−16.28	27.76	0.54	297.0	7.91 ± 0.08
NGC 3109	−15.30	25.72	0.49	1876.7	7.74 ± 0.33
NGC 4214	−18.04	28.25	0.46	368.8	8.24 ± 0.12
NGC 5408	−15.81	27.76	0.49	59.20	8.01 ± 0.02
NGC 6822	−14.95	23.46	0.59	2367.1	8.25 ± 0.11
Sextans A	−14.04	25.84	0.38	208.8	7.55 ± 0.11
Sextans B	−14.02	25.67	0.51	102.4	8.12 ± 0.12
SMC	−16.56	19.06	0.59	8.99×10^5	8.03 ± 0.10
UGC 6456	−13.90	28.31	0.38	16.20	7.64 ± 0.13
WLM	−13.92	24.86	0.42	299.8	7.78 ± 0.16

^a Its optical appearance shares similarities with blue compact dwarfs (Richer et al. 2001).

^b This is a post-starburst dwarf galaxy (Heckman et al. 1995; Greggio et al. 1998).

Note. — Column (1): Galaxy name in alphabetical order Column (2): Absolute magnitude in B . Column (3): Extinction-corrected distance modulus. Column (4): Total dereddened $B - V$ colour. Column (5): Integrated flux density at the 21-cm H I line. Column (6): Logarithm of the oxygen abundance by number.

Table 2. Revisions to distances for the sample of dIs in the field.

Galaxy (1)	New/Update (2)	Method ^a (3)	References (4)
DDO 187	New	Ceph, TRGB	1, 2
GR 8	Update	Ceph, TRGB	3, 4
Holmberg II	Update	Ceph	5
IC 10	Update	Ceph, TRGB	6, 7, 8
IC 1613	Update	TRGB	9
Leo A	Update ^b	Ceph, TRGB	10, 11
LMC	Update	SN87, TRGB	12, 13
NGC 2366	Update	Ceph	14
NGC 3109	Update	Ceph, TRGB	15, 16
NGC 6822	Update	Ceph, TRGB	17
UGC 6456	Update	TRGB	18, 19
Sextans A	Update	Ceph, TRGB	20
Sextans B	Update	Ceph, TRGB	21
WLM	Update	TRGB	22

^a Distance method: “Ceph” denotes Cepheid variables, “SN87” denotes the expanding ring of the supernova remnant SN1987A, and “TRGB” denotes the tip of the red giant branch.

^b For Leo A, Tolstoy et al. (1998) dispute the claim of detected Cepheids by Hoessel et al. (1994). The result adopted here is the average of the Cepheid and the TRGB distances obtained by Tolstoy et al. (1998).

Note. — Column (1) : Galaxy name in alphabetical order. Column (2) : New addition or update. Column (3) : Method by which distances are obtained. Column (4) : References.

References. — (1) Hoessel et al. (1998b); (2) Aparicio et al. (2000); (3) Dohm-Palmer et al. (1998); (4) Tolstoy et al. (1995a); (5) Hoessel et al. (1998a); (6) Saha et al. (1996); (7) Sakai et al. (1999); (8) Wilson et al. (1996); (9) Cole et al. (1999); (10) Hoessel et al. (1994); (11) Tolstoy et al. (1998); (12) Panagia (1999); (13) Sakai et al. (2000); (14) Tolstoy et al. (1995b); (15) Minniti et al. (1999); (16) Musella et al. (1997); (17) Gallart et al. (1996); (18) Lynds et al. (1998); (19) Schulte-Ladbeck et al. (1998); (20) Sakai et al. (1996); (21) Sakai et al. (1997); (22) Minniti & Zijlstra (1997).

Table 3. Revisions to oxygen abundances for the sample of dIs in the field.

Galaxy (1)	New/Update (2)	References (3)
DDO 187	New	1
Holmberg II	Update	2
IC 10	Update	2
IC 1613	Update	3
IC 2574	Update	4
NGC 1560	Update	2
NGC 1569	Update	5
NGC 2366	Update	6, 7
NGC 3109	Update	2
NGC 4214	Update	8
NGC 6822	Update	9
UGC 6456	Update	2, 7, 10
WLM	Update	11

Note. — Column (1) : Galaxy name in alphabetical order. Column (2) : New addition or update. Column (3) : References.

References. — (1) van Zee, Haynes, & Salzer (1997); (2) present work; (3) Kingsburgh & Barlow (1995); (4) Miller & Hodge (1996); (5) Kobulnicky & Skillman (1997); (6) González-Delgado et al. (1994); (7) Izotov, Thuan, & Lipovetsky (1997); (8) Kobulnicky & Skillman (1996); (9) Miller (1996); (10) Hunter & Hoffman (1999); (11) Hodge & Miller (1995).

Table 4: Instrument configurations at Steward and Observatorio Astronómico Nacional (OAN).

Property	Steward (blue)	Steward (red)	OAN (red)
Telescope			
Aperture	2.3 metre Bok		2.1 metre
Focus	f/9.0		f/7.5
Spectrograph	Boller & Chivens		Boller & Chivens
CCD			
Type	Texas Instruments		Tektronix
Total area	800 pix \times 800 pix		1024 pix \times 1024 pix
Usable area	800 pix \times 350 pix		1024 pix \times 400 pix
Pixel size	15 μm		24 μm
Image scale	0.8 arcsec pix $^{-1}$		0.92 arcsec pix $^{-1}$
Gain	2.8 e^- ADU $^{-1}$		1.22 e^- ADU $^{-1}$
Read-noise (rms)	7.4 e^-		3 e^-
Grating, Long slit			
Groove density	600 lines mm $^{-1}$	600 lines mm $^{-1}$	300 lines mm $^{-1}$
Blaze λ (1st order)	3568 \AA	6690 \AA	5000 \AA
Dispersion	1.89 \AA pix $^{-1}$	3.72 \AA pix $^{-1}$	3.96 \AA pix $^{-1}$
Effective λ range	3650–5100 \AA	4200–7200 \AA	3450–7450 \AA
Slit width	2.5 arcsec	4.5 arcsec	2.2 arcsec

Table 5. Log of Observations.

Galaxy (1)	Obs. (2)	Date (UT) (3)	N_{exp} (4)	t_{total} (s) (5)	[O III] $\lambda 4363$ (6)	δ (mag) (7)
Holmberg II	Steward	1992 Mar 23	$1 \times 300 + 3 \times 1200$	3900	detected	3.7 %
IC 10	Steward	1991 Oct 15	$1 \times 60 + 3 \times 1800$	5460	detected	2.2 %
IC 10	OAN ^a	1994 Nov 30	1×1200	1200	...	3.0 %
NGC 1560	Steward	1991 Oct 15	3×1800	5400	upper limits	2.2 %
NGC 1560 “1” (NE) ^b	Steward ^a	1992 Jan 27	1×1200	1200	...	2.2 %
NGC 1560 “2” (SW) ^c	Steward ^a	1992 Jan 27	1×900	900	...	2.2 %
NGC 3109	Steward	1992 Mar 23	$1 \times 300 + 4 \times 1200$	5100	detected	3.7 %
UGC 6456	Steward	1992 Mar 23	$1 \times 300 + 4 \times 900$	3900	detected	3.7 %

^aDesigned to measure ratio of H α /H β fluxes.

^bOne exposure for slit placement to the northeast of the main body of the galaxy.

^cOne exposure for slit placement to the southwest of the main body of the galaxy.

Note. — Column (1): Galaxy name. Column (2): Observatory. Column (3): Date. Column (4): Number of exposures obtained and the length of each exposure in seconds. Column (5): Total exposure time. Column (6): [O III] $\lambda 4363$ detection. Column (7): Relative root-mean-square error in the sensitivity function obtained from observations of standard stars.

Table 6. Identification of H II regions in Holmberg II (Ho II).

H II Region (1)	[O III] λ 4363 (2)	HSK94 (3)	HG85 (4)
Ho II-1	upper limit	67	6
Ho II-2 ^a	upper limit	67	6
Ho II-3	upper limit	67	6
Ho II-4	upper limit	69?	...
Ho II-5	detected	70	5
Ho II-6	upper limit	73	4
Ho II-7 ^b	detected	73	4
Ho II-8	detected	73	4
Ho II-9	detected	71	3

^a The H II region Ho II-2 encompasses two separate H II regions 1 and 3. Subsequent line intensities and derived quantities for Ho II-2 are not independent of the two latter H II regions.

^b The H II region Ho II-7 encompasses two separate H II regions 6 and 8. Subsequent line intensities and derived quantities for Ho II-7 are not independent of the two latter H II regions.

Note. — Column (1): H II region. The H II region number increases along the slit towards the north. Column (2): [O III] λ 4363 detection. Columns (3) and (4): corresponding H II regions identified by Hodge, Strobel, & Kennicutt (1994, Figure 2, HSK94) and Hunter & Gallagher (1985, Figure 1 for DDO 50, HG85), respectively.

Table 7. Identification of H II regions in IC 10.

H II Region (1)	[O III] λ 4363 (2)	LPRSTP (3)	HL90 (4)
IC 10-1 ^a	detected	1	111c,e
IC 10-2	detected	...	111c
IC 10-3	detected	...	111e
IC 10-4 ^b	upper limit	...	111b
IC 10-5	upper limit	...	106a
IC 10-6 ^c	106 south, diffuse

^a The H II region IC 10-1 encompasses two separate H II regions 2 and 3. Subsequent line intensities and derived quantities for IC 10-1 are not independent of the two latter H II regions.

^b Light from this H II region may include a contribution from the neighbouring H II region 111a (Hodge & Lee 1990).

^c The observed spectrum was not of sufficient quality to be included in the analysis.

Note. — Column (1): H II region. The H II region number increases along the slit towards the south. Column (2): [O III] λ 4363 detection. Columns (3) and (4): corresponding H II regions identified by Lequeux et al. (1979, Figure 1, LPRSTP) and Hodge & Lee (1990, Figure 2, HL90), respectively.

Table 8. Identification of H II regions in NGC 1560.

H II Region (1)	[O III] λ 4363 (2)	Notes (3)
NGC 1560-1	upper limit	MLM #1 ^a
NGC 1560-2	upper limit	bright
NGC 1560-3	upper limit	faint
NGC 1560-4 ^b	upper limit	faint
NGC 1560-5	upper limit	faint
NGC 1560-6	not detected	very faint
NGC 1560-7	not detected	very faint

^a Identified as H II region #1 in the H α image by M. L. McCall.

^b The H II region NGC 1560-4 encompasses two separate H II regions 3 and 5. Subsequent line intensities and derived quantities for NGC 1560-4 are not independent of the two latter H II regions.

Note. — Column (1): H II region. The H II region number increases along the slit towards the northeast. Column (2): [O III] λ 4363 detection. Column (3): comments about the relative brightness observed for each H II region.

Table 9. Identification of H II regions in NGC 3109.

H II Region (1)	[O III] λ 4363 (2)	Notes (3)	RM92 (4)
NGC 3109 – 1	no H γ	very faint	...
NGC 3109 – 2	no [O III] λ 4959	very faint	...
NGC 3109 – 3 ^a	detected	bright	5
NGC 3109 – 4 ^b	upper limit	bright	5

^a The extraction window was narrow (6 pixels) to isolate the signal from the H II region.

^b The extraction window was wide (20 pixels), which included the spectrum of an early-type field star adjacent to the H II region.

Note. — Column (1): H II region. The H II region number increases along the slit towards the north. Column (2): [O III] λ 4363 detection. Column (3): notes about the H II regions. Column (4): corresponding H II region identified by Richer & McCall (1992, Fig. 1, RM92).

Table 10. Identification of H II regions in UGC 6456.

H II Region (1)	[O III] λ 4363 (2)	Lynds et al. 1998 (3)	Tully et al. 1981 (4)
UGC 6456 – 1	detected	5	2nd clump in slit
UGC 6456 – 2	detected	1	brightest clump in slit

Note. — Column (1): H II region. The H II region number increases along the slit towards the east. Column (2): [O III] λ 4363 detection. Columns (3) and (4): corresponding H II regions identified by Lynds et al. (1998, Figure 2) and Tully et al. (1981, Figure 2), respectively.

Table 11: Observed and corrected line ratios for Holmberg II.

Identification (Å)	H _β II-1		H _β II-2		H _β II-3	
	F	I	F	I	F	I
[O II] 3727	447 ± 11	443 ± 48	259.3 ± 4.7	257 ± 22	186.7 ± 4.5	185 ± 16
[Ne III] 3869	48.8 ± 4.8	48.3 ± 8.1	34.3 ± 2.6	34.0 ± 4.4	29.5 ± 2.6	29.2 ± 4.1
He I + H _β 3889	34.1 ± 4.6	36.6 ± 8.0	26.4 ± 2.5	28.8 ± 4.9	25.1 ± 2.6	27.3 ± 4.6
[Ne III] + He 3970	48.6 ± 4.8	50.4 ± 9.0	37.7 ± 2.6	39.1 ± 4.6	33.3 ± 3.0	34.5 ± 5.2
H _δ 4101	44.4 ± 7.7	46 ± 12	37.2 ± 3.7	38.9 ± 6.2	34.8 ± 3.3	36.5 ± 5.7
H _γ 4340	61.2 ± 4.4	61.6 ± 9.3	58.4 ± 2.4	59.3 ± 6.1	57.1 ± 2.4	58.2 ± 6.0
[O III] 4363	< 9.1 (2 σ)	< 6.8 (2 σ)	8.3 ± 1.9	8.2 ± 2.3	9.0 ± 2.0	8.9 ± 2.4
H _β 4861	100.0 ± 4.5	100.0 ± 6.3	100.0 ± 2.2	100.0 ± 4.5	100.0 ± 2.1	100.0 ± 4.4
[O III] 4959	87.8 ± 5.4	87 ± 12	79.7 ± 4.8	79.0 ± 9.1	69.4 ± 5.2	68.7 ± 8.8
[O III] 5007	260.2 ± 6.6	258 ± 28	192.9 ± 5.8	191 ± 18	159.8 ± 6.1	158 ± 15
Identification (Å)	H _β II-4		H _β II-5		H _β II-6	
	F	I	F	I	F	I
[O II] 3727	251.1 ± 8.1	246 ± 25	191.4 ± 2.6	188 ± 15	261.3 ± 3.2	257 ± 20
[Ne III] 3869	26.7 ± 1.2	26.2 ± 2.6	23.2 ± 1.9	22.8 ± 3.0
He I + H _β 3889	17.2 ± 1.1	21.1 ± 2.7	21.0 ± 1.9	24.3 ± 3.8
[Ne III] + He 3970	18.7 ± 3.9	21.7 ± 6.5	21.9 ± 1.6	25.2 ± 3.3	21.5 ± 2.6	24.6 ± 4.5
H _δ 4101	20.2 ± 3.8	22.7 ± 6.2	24.3 ± 1.5	27.4 ± 3.3	29.7 ± 2.2	32.2 ± 4.2
H _γ 4340	50.0 ± 2.7	51.5 ± 6.3	47.72 ± 0.94	49.8 ± 4.1	43.8 ± 2.4	45.6 ± 5.1
[O III] 4363	< 4.7 (2 σ)	< 3.5 (2 σ)	6.02 ± 0.75	5.9 ± 1.0	< 3.0 (2 σ)	< 2.2 (2 σ)
He I 4472	2.65 ± 0.91	2.6 ± 1.0	4.1 ± 1.2	4.0 ± 1.3
He II 4686	2.90 ± 0.59	2.85 ± 0.71
H _β 4861	100.0 ± 3.2	100.0 ± 5.2	100.0 ± 1.2	100.0 ± 4.0	100.0 ± 1.2	100.0 ± 4.0
[O III] 4959	41.9 ± 3.3	41.1 ± 5.7	96.0 ± 2.2	94.1 ± 7.7	72.7 ± 1.8	72.5 ± 6.0
[O III] 5007	139.2 ± 4.1	137 ± 14	269.5 ± 2.7	264 ± 21	213.5 ± 2.2	211 ± 16
Identification (Å)	H _β II-7		H _β II-8		H _β II-9	
	F	I	F	I	F	I
[O II] 3727	239.2 ± 2.1	235 ± 18	221.0 ± 2.0	217 ± 17	144.8 ± 2.2	143 ± 12
[Ne III] 3869	23.4 ± 1.1	23.0 ± 2.3	22.5 ± 1.2	22.1 ± 2.3	18.9 ± 1.1	18.6 ± 2.1
He I + H _β 3889	20.3 ± 1.1	22.8 ± 2.5	19.5 ± 1.2	21.4 ± 2.6	15.1 ± 1.1	16.7 ± 2.2
[Ne III] + He 3970	22.2 ± 1.7	24.6 ± 3.3	22.4 ± 1.5	24.2 ± 3.0	17.54 ± 0.70	19.1 ± 1.9
H _δ 4101	27.3 ± 1.2	29.5 ± 3.0	25.5 ± 1.1	27.5 ± 2.7	21.56 ± 0.73	23.2 ± 2.2
H _γ 4340	47.3 ± 1.4	48.8 ± 4.3	49.5 ± 1.2	50.8 ± 4.3	42.85 ± 0.86	43.9 ± 3.7
[O III] 4363	3.2 ± 1.1	3.2 ± 1.2	4.30 ± 0.92	4.2 ± 1.1	5.69 ± 0.69	5.61 ± 0.94
He I 4472	2.95 ± 0.90	2.9 ± 1.0	3.43 ± 0.90	3.4 ± 1.0	3.11 ± 0.64	3.07 ± 0.77
H _β 4861	100.00 ± 0.91	100.0 ± 3.9	100.0 ± 1.0	100.0 ± 3.9	100.0 ± 1.4	100.0 ± 4.0
[O III] 4959	73.7 ± 1.2	72.5 ± 5.7	75.0 ± 1.3	73.6 ± 5.9	105.3 ± 3.9	103.9 ± 9.6
[O III] 5007	215.1 ± 1.5	211 ± 16	217.6 ± 1.5	214 ± 16	300.7 ± 4.8	297 ± 24

Note. — Wavelengths are listed in Å. F is the observed flux ratio with respect to H_β. I is the corrected intensity ratio, corrected only for underlying Balmer absorption. The reddening was assumed to be zero. The errors in the observed line ratios account for the errors in the fits to the line profiles, the surrounding continua, and the relative error in the sensitivity function listed in Table 5. Flux errors in the H_β reference line are not included in the ratio relative to H_β. Errors in the corrected line ratios account for errors in the specified line and in the H_β reference line.

Table 12: Observed and corrected line ratios for IC 10 at OAN.

Identification (Å)	IC 10-1		IC 10-2		IC 10-3	
	<i>F</i>	<i>I</i>	<i>F</i>	<i>I</i>	<i>F</i>	<i>I</i>
H β 4861	100.0 \pm 2.2	100.0 \pm 3.8	100.0 \pm 1.7	100.0 \pm 3.5	100.0 \pm 3.9	100.0 \pm 5.1
H α 6563	628.0 \pm 4.0	286 \pm 20	620.0 \pm 3.4	286 \pm 19	676.0 \pm 5.3	286 \pm 24
<i>E(B - V)</i> (mag)	+0.788 \pm 0.070		+0.773 \pm 0.067		+0.862 \pm 0.083	
IC 10-4						
Identification (Å)	<i>F</i>		<i>I</i>		<i>F</i>	
	100.0 \pm 4.5	100.0 \pm 5.7	100.0 \pm 5.3	100.0 \pm 6.3		
H β 4861	703.0 \pm 7.7		286 \pm 26	961.0 \pm 8.6	286 \pm 27	
<i>E(B - V)</i> (mag)	+0.897 \pm 0.091		+1.215 \pm 0.096			

Note. — Wavelengths are listed in Å. *F* is the observed flux ratio with respect to H β . *I* is the intensity ratio corrected for underlying Balmer absorption and for reddening.

Table 13: Observed and corrected line ratios for IC 10 at Steward.

Identification (Å)	IC 10-1		IC 10-2		IC 10-3		
	<i>F</i>	<i>I</i>	<i>F</i>	<i>I</i>	<i>F</i>	<i>I</i>	
[O II] 3727	68.5 ± 1.1	198 ± 30	61.9 ± 1.3	175 ± 26	98.7 ± 2.6	312 ± 56	
[Ne III] 3869	12.28 ± 0.70	29.6 ± 5.0	12.64 ± 0.69	30.0 ± 4.9	12.8 ± 1.9	33.2 ± 9.0	
He I + H8 3889	8.64 ± 0.67	25.8 ± 5.2	9.36 ± 0.66	26.5 ± 5.0	7.5 ± 1.5	27 ± 11	
[Ne III] + He 3970	10.99 ± 0.63	28.4 ± 4.8	11.21 ± 0.67	28.1 ± 4.7	10.6 ± 1.2	31.1 ± 8.0	
H δ 4101	15.32 ± 0.49	32.6 ± 4.2	15.49 ± 0.49	32.3 ± 4.0	15.5 ± 1.2	35.8 ± 6.7	
H γ 4340	34.18 ± 0.40	53.5 ± 4.8	35.28 ± 0.41	54.5 ± 4.7	29.36 ± 0.83	48.9 ± 5.4	
[O III] 4363	1.65 ± 0.32	2.37 ± 0.60	1.53 ± 0.33	2.20 ± 0.60	2.77 ± 0.73	4.1 ± 1.4	
He I 4472	3.48 ± 0.31	4.55 ± 0.66	3.46 ± 0.32	4.52 ± 0.66	3.71 ± 0.71	4.9 ± 1.3	
He II 4686	1.44 ± 0.53	1.60 ± 0.65	
H β 4861	100.0 ± 1.3	100.0 ± 2.7	100.0 ± 1.3	100.0 ± 2.6	100.0 ± 1.7	100.0 ± 2.9	
[O III] 4959	134.5 ± 5.9	123.4 ± 8.6	136.7 ± 5.7	126.9 ± 8.6	127.7 ± 6.3	115.3 ± 8.8	
[O III] 5007	404.8 ± 7.4	360 ± 17	409.1 ± 7.2	366 ± 17	391.6 ± 7.9	342 ± 17	
IC 10-4		IC 10-5					
Identification (Å)	<i>F</i>	<i>I</i>	<i>F</i>	<i>I</i>			
[O II] 3727	154.2 ± 2.9	517 ± 98	105.0 ± 6.2	550 ± 130			
[Ne III] 3869			
He I + H8 3889	9.2 ± 1.5	29.4 ± 9.8			
[Ne III] + He 3970	12.6 ± 2.1	34 ± 11	12.3 ± 2.8	44 ± 17			
H δ 4101	10.9 ± 1.3	26.5 ± 6.8	20.4 ± 2.6	56 ± 15			
H γ 4340	32.0 ± 1.3	52.9 ± 6.9	29.0 ± 2.6	55 ± 11			
[O III] 4363	< 1.6 (2 σ)	< 2.5 (2 σ)	< 4.8 (2 σ)	< 8.7 (2 σ)			
He I 4472	2.04 ± 0.60	2.8 ± 1.0			
He II 4686			
H β 4861	100.0 ± 2.5	100.0 ± 3.5	100.0 ± 3.6	100.0 ± 4.5			
[O III] 4959	63.3 ± 4.3	57.6 ± 5.7	102.9 ± 9.2	92 ± 12			
[O III] 5007	194.8 ± 5.4	171 ± 10	326.1 ± 11.8	278 ± 21			

Note. — Wavelengths are listed in Å. *F* is the observed flux ratio with respect to H β . *I* is the corrected intensity ratio, corrected only for underlying Balmer absorption. The reddening was assumed to be zero. The errors in the observed line ratios account for the errors in the fits to the line profiles, the surrounding continua, and the relative error in the sensitivity function listed in Table 5. Flux errors in the H β reference line are not included in the ratio relative to H β . Errors in the corrected line ratios account for errors in the specified line and in the H β reference line.

Table 14: Observed and corrected line ratios for NGC 1560 (red spectra).

Identification (Å)	NGC 1560–1 NE		NGC 1560–2 NE			
	<i>F</i>	<i>I</i>	<i>F</i>	<i>I</i>	<i>F</i>	<i>I</i>
H β 4861	100.0 \pm 6.3	100.0 \pm 7.0	100 \pm 21	100 \pm 24		
H α 6563	396 \pm 14	286 \pm 44	183 \pm 10	286 \pm 86		
$E(B - V)$ (mag)	+0.33 \pm 0.15		-0.47 \pm 0.29			
Identification (Å)	NGC 1560–1 SW		NGC 1560–2 SW		NGC 1560–3 SW	
	<i>F</i>	<i>I</i>	<i>F</i>	<i>I</i>	<i>F</i>	<i>I</i>
H β 4861	100.0 \pm 8.3	100 \pm 10	100.0 \pm 8.2	100 \pm 10	100.0 \pm 8.5	100 \pm 10
H α 6563	523 \pm 15	286 \pm 39	465 \pm 15	286 \pm 40	397 \pm 17	286 \pm 43
$E(B - V)$ (mag)	+0.48 \pm 0.14		+0.38 \pm 0.14		+0.24 \pm 0.15	
Identification (Å)	NGC 1560–6 SW		NGC 1560–7 SW			
	<i>F</i>	<i>I</i>	<i>F</i>	<i>I</i>	<i>F</i>	<i>I</i>
H β 4861	100.0 \pm 7.9	100.0 \pm 8.9	100 \pm 34	100 \pm 46		
H α 6563	445 \pm 13	286 \pm 36	556 \pm 15	286 \pm 155		
$E(B - V)$ (mag)	+0.38 \pm 0.13		+0.56 \pm 0.51			

Note. — Wavelengths are listed in Å. *F* is the observed flux ratio with respect to H β . *I* is the intensity ratio corrected for underlying Balmer absorption and for reddening. The reddening adopted for NGC 1560 is the average of the reddening values for H II regions 1 NE, 1 SW, 2 SW, 3 SW, and 6 SW.

Table 15: Observed and corrected line ratios for NGC 1560 (blue spectra).

Identification (Å)	NGC 1560-1		NGC 1560-2		NGC 1560-3	
	F	I	F	I	F	I
[O II] 3727	154.3 ± 6.7	254 ± 22	224.7 ± 4.8	359 ± 23	209 ± 20	338 ± 56
[Ne III] 3869	8.9 ± 3.8	13.5 ± 6.2	13.0 ± 2.1	19.2 ± 3.8	31.8 ± 7.2	48 ± 14
He I + H δ 3889	19.2 ± 2.4	31.6 ± 5.6
[Ne III] + He 3970	12.2 ± 2.7	17.0 ± 5.2	10.7 ± 1.8	18.8 ± 4.5
H δ 4101	31.4 ± 4.9	40.9 ± 8.4	21.0 ± 1.7	30.8 ± 4.0	26.2 ± 5.6	38 ± 12
H γ 4340	40.7 ± 2.1	48.5 ± 4.6	43.9 ± 1.5	54.4 ± 4.3	50.0 ± 5.0	61 ± 11
[O III] 4363	< 2.8 (2 σ)	< 3.4 (2 σ)	< 2.8 (2 σ)	< 3.3 (2 σ)	< 11.5 (2 σ)	< 13.6 (2 σ)
He I 4472	4.02 ± 0.75	4.5 ± 1.0
H β 4861	100.0 ± 2.6	100.0 ± 3.6	100.0 ± 2.4	100.0 ± 3.4	100.0 ± 5.6	100.0 ± 7.0
[O III] 4959	124.6 ± 4.7	122.3 ± 9.8	81.8 ± 5.2	78.1 ± 8.0	150 ± 11	145 ± 21
[O III] 5007	324.8 ± 5.8	315 ± 20	238.1 ± 6.6	224 ± 16	426 ± 14	407 ± 44
NGC 1560-4						
Identification (Å)	NGC 1560-4		NGC 1560-5		NGC 1560-6	
	F	I	F	I	F	I
[O II] 3727	220 ± 18	363 ± 49	254 ± 18	423 ± 56	295 ± 37	385 ± 91
[Ne III] 3869	19.8 ± 6.9	30 ± 12
He I + H δ 3889	38.7 ± 5.9	58 ± 13
[Ne III] + He 3970	23.2 ± 5.3	33.9 ± 9.0	27.8 ± 6.7	39 ± 13
H δ 4101	34.8 ± 6.1	46 ± 11	29.3 ± 5.7	38 ± 10
H γ 4340	52.1 ± 3.9	61.3 ± 8.4	44.5 ± 4.1	51.6 ± 8.4
[O III] 4363	< 6.7 (2 σ)	< 8.1 (2 σ)	< 4.4 (2 σ)	< 5.3 (2 σ)
H β 4861	100.0 ± 4.5	100.0 ± 5.3	100.0 ± 5.2	100.0 ± 6.0	100.0 ± 8.5	100 ± 11
[O III] 4959	110.5 ± 8.2	109 ± 14	58.5 ± 4.9	58.3 ± 8.5	40.3 ± 6.8	31.4 ± 8.7
[O III] 5007	318 ± 11	310 ± 29	175.8 ± 6.2	173 ± 18	130.1 ± 9.4	100 ± 18
NGC 1560-7						
Identification (Å)	NGC 1560-7					
	F	I				
[O II] 3727	182.1 ± 67.2	240 ± 140				
H β 4861	100.0 ± 16.2	100 ± 20				
[O III] 4959	37.1 ± 17.7	29 ± 20				
[O III] 5007	214.02 ± 23.2	163 ± 52				

Note. — Wavelengths are listed in Å. F is the observed flux ratio with respect to H β . I is the corrected intensity ratio, corrected only for underlying Balmer absorption. The reddening was assumed to be zero. The errors in the observed line ratios account for the errors in the fits to the line profiles, the surrounding continua, and the relative error in the sensitivity function listed in Table 5. Flux errors in the H β reference line are not included in the ratio relative to H β . Errors in the corrected line ratios account for errors in the specified line and in the H β reference line.

Table 16: Observed and corrected line ratios for NGC 3109.

Identification (Å)	NGC 3109-1		NGC 3109-2	
	<i>F</i>	<i>I</i>	<i>F</i>	<i>I</i>
[O II] 3727	418 ± 77	420 ± 200	385 ± 11	380 ± 44
[Ne III] 3869
He I + H8 3889
[Ne III] + He 3970
H δ 4101
H γ 4340	42.3 ± 5.6	45 ± 12
[O III] 4363
H β 4861	100 ± 26	100 ± 28	100.0 ± 5.2	100 ± 6.8
[O III] 4959	41 ± 23	41 ± 36
[O III] 5007	202 ± 30	204 ± 90	24.2 ± 4.6	23.9 ± 6.2
NGC 3109-3				
Identification (Å)	NGC 3109-3		NGC 3109-4	
	<i>F</i>	<i>I</i>	<i>F</i>	<i>I</i>
[O II] 3727	227.5 ± 6.2	220 ± 20	304.8 ± 7.4	283 ± 26
[Ne III] 3869	10.9 ± 2.1	10.5 ± 2.5
He I + H8 3889	16.5 ± 2.8	21.1 ± 5.6
[Ne III] + He 3970	16.7 ± 3.2	20.9 ± 6.1
H δ 4101	20.9 ± 3.6	25.0 ± 6.4	17.3 ± 2.7	27.1 ± 7.6
H γ 4340	45.3 ± 2.4	47.7 ± 5.5	41.1 ± 3.2	47.4 ± 7.1
[O III] 4363	5.7 ± 2.0	5.5 ± 2.2	< 6.5 (2 σ)	< 6.0 (2 σ)
H β 4861	100.0 ± 2.2	100.0 ± 4.4	100.0 ± 2.5	100.0 ± 4.7
[O III] 4959	105.7 ± 3.3	102.3 ± 9.5	100.6 ± 3.4	93.3 ± 9.1
[O III] 5007	313.4 ± 4.1	303 ± 25	280.6 ± 4.1	260 ± 23

Note. — Wavelengths are listed in Å. *F* is the observed flux ratio with respect to H β ≡ 100 and *I* is the intensity ratio corrected only for underlying Balmer absorption. The reddening was assumed to be zero. The errors in the observed lines account only for the errors in the fits to the line profiles and surrounding continua, and the relative error in the sensitivity function (Table 5). Flux errors in the H β reference line are not included in the ratio relative to H β . However, errors in the corrected line ratios account for flux errors in both the specified line and in the reference line.

Table 17: Observed and corrected line ratios for UGC 6456.

Identification (Å)	UGC 6456-1		UGC 6456-2	
	<i>F</i>	<i>I</i>	<i>F</i>	<i>I</i>
[O II] 3727	136.8 ± 6.1	133 ± 16	116.2 ± 1.9	114.6 ± 9.2
[Ne III] 3869	12.5 ± 2.5	12.1 ± 3.2	25.7 ± 1.2	25.3 ± 2.5
He I + H8 3889	12.9 ± 2.5	18.0 ± 5.9	16.4 ± 1.1	18.5 ± 2.3
[Ne III] + He 3970	19.9 ± 1.0	22.0 ± 2.4
Hδ 4101	21.7 ± 3.0	25.8 ± 6.0	26.0 ± 1.1	27.9 ± 2.9
Hγ 4340	46.2 ± 2.7	48.5 ± 6.6	50.2 ± 1.4	51.3 ± 4.6
[O III] 4363	8.6 ± 2.2	8.3 ± 2.7	8.3 ± 1.1	8.2 ± 1.5
He I 4472	4.41 ± 0.89	4.4 ± 1.1
He II 4686	1.54 ± 0.58	1.52 ± 0.61
Hβ 4861	100.0 ± 4.3	100.0 ± 6.0	100.0 ± 1.2	100.0 ± 4.0
[O III] 4959	87.9 ± 3.3	85.3 ± 9.7	112.0 ± 3.5	110.5 ± 9.8
[O III] 5007	237.3 ± 4.1	231 ± 23	308.5 ± 4.4	304 ± 24

Note. — Wavelengths are listed in Å. *F* is the observed flux ratio with respect to H β ≡ 100 and *I* is the intensity ratio corrected only for underlying Balmer absorption. The reddening was assumed to be zero. The errors in the observed lines account only for the errors in the fits to the line profiles and surrounding continua, and the relative error in the sensitivity function (Table 5). Flux errors in the H β reference line are not included in the ratio relative to H β . However, errors in the corrected line ratios account for flux errors in both the specified line and in the reference line.

Table 18: Observed and corrected line ratios for DDO 187.

Identification (Å)	DDO 187-1		DDO 187-2	
	<i>F</i>	<i>I</i>	<i>F</i>	<i>I</i>
[O II] 3727	180 ± 8.4	175.2 ± 8.4	256 ± 15	237 ± 15
[Ne III] 3869	27.5 ± 1.4	26.8 ± 1.4
H γ 4340	44.3 ± 1.8	44.3 ± 1.8	35.3 ± 2.7	35.3 ± 2.7
[O III] 4363	2.7 ± 0.6	2.6 ± 0.6
H β 4861	100.0 ± 3.7	100.0 ± 3.7	100.0 ± 4.8	100.0 ± 4.8
[O III] 4959	64.5 ± 2.4	62.8 ± 2.4	16.6 ± 2.3	15.4 ± 2.3
[O III] 5007	187.8 ± 6.8	182.8 ± 6.8	47 ± 3	43 ± 3
H α 6563	274 ± 13	274 ± 13	270 ± 16	270 ± 16
[N II] 6583	4.3 ± 0.4	4.2 ± 0.4	5.7 ± 0.7	5.3 ± 0.7
He I 6678	1.9 ± 0.3	1.9 ± 0.3
[S II] 6716	78.0 ± 0.5	75.9 ± 0.5	15.2 ± 1.1	14.1 ± 1.1
[S II] 6731	63.0 ± 0.4	61.3 ± 0.4	11.6 ± 0.9	10.7 ± 0.9
He I 7065	1.6 ± 0.3	1.6 ± 0.3
[Ar III] 7136	3.2 ± 0.3	3.1 ± 0.3

Note. — Observed and re-analyzed line ratios for DDO 187. Wavelengths are listed in Å. *F* is the observed flux ratio with respect to H β = 100 (van Zee, Haynes, & Salzer 1997) and *I* is the intensity ratio corrected for underlying Balmer absorption with an equivalent width of 2 Å. The reddening was assumed to be zero.

Table 19. Derived properties for H II regions in Holmberg II, IC 10, NGC 1560, NGC 3109, UGC 6456, and DDO 187.

H II Region	$I(\text{H}\beta)$ (ergs s^{-1} cm^{-2})	Derived $E(B - V)$ (mag)	Adopted $E(B - V)$ (mag)	$W_e(\text{H}\beta)$ (Å)	$T_e(\text{O}^{+2})$ (K)	$12 + \log(\text{O}/\text{H})$ (dex)
(1)	(2)	(3)	(4)	(5)	(6)	(7)
Ho II-1	$(1.97 \pm 0.12) \times 10^{-15}$	-0.59 ± 0.29	0	209 ± 79	< 17400	> 7.64
Ho II-2	$(6.85 \pm 0.31) \times 10^{-15}$	-0.46 ± 0.20	0	218 ± 42	< 23500	> 7.17
Ho II-3	$(4.47 \pm 0.20) \times 10^{-15}$	-0.42 ± 0.20	0	201 ± 35	< 29000	> 6.89
Ho II-4	$(3.24 \pm 0.17) \times 10^{-15}$	-0.18 ± 0.24	0	104 ± 14	< 17300	> 7.37
Ho II-5	$(2.144 \pm 0.085) \times 10^{-14}$	-0.12 ± 0.16	0	101.9 ± 5.0	16000 ± 1300	7.56 ± 0.13
Ho II-6	$(9.46 \pm 0.37) \times 10^{-15}$	$+0.05 \pm 0.22$	0	113.8 ± 5.8	< 11700	> 7.97
Ho II-7	$(2.099 \pm 0.081) \times 10^{-14}$	-0.08 ± 0.17	0	113.5 ± 4.6	13400 ± 2100	7.76 ± 0.25
Ho II-8	$(1.147 \pm 0.045) \times 10^{-14}$	-0.16 ± 0.17	0	112.3 ± 5.0	15100 ± 1800	7.60 ± 0.18
Ho II-9	$(3.24 \pm 0.13) \times 10^{-14}$	$+0.12 \pm 0.16$	0	155 ± 12	14800 ± 1100	7.65 ± 0.13
IC 10-1	$(1.58 \pm 0.41) \times 10^{-11}$	$+0.788 \pm 0.070^a$	$+0.788$	88.5 ± 3.9	10100 ± 560	8.29 ± 0.13
IC 10-2	$(1.18 \pm 0.29) \times 10^{-11}$	$+0.773 \pm 0.067^a$	$+0.773$	101.0 ± 4.7	9800 ± 580	8.32 ± 0.14^b
IC 10-3	$(3.6 \pm 1.1) \times 10^{-12}$	$+0.862 \pm 0.083^a$	$+0.862$	60.5 ± 2.4	12300 ± 1100	8.05 ± 0.18
IC 10-4	$(6.3 \pm 2.1) \times 10^{-12}$	$+0.897 \pm 0.091^a$	$+0.897$	92.6 ± 7.6	< 13200	> 7.96
IC 10-5	$(1.09 \pm 0.40) \times 10^{-11}$	$+1.215 \pm 0.096^a$	$+1.215$	154 ± 28	< 19100	> 7.60
NGC 1560-1	$(1.245 \pm 0.045) \times 10^{-14}$...	$+0.354^c$...	d	< 11900
NGC 1560-2	$(1.725 \pm 0.059) \times 10^{-14}$...	$+0.354^c$	111 ± 11	< 13300	> 7.89
NGC 1560-3	$(7.73 \pm 0.54) \times 10^{-15}$...	$+0.354^c$	460 ± 370	< 19900	> 7.55
NGC 1560-4	$(1.450 \pm 0.077) \times 10^{-14}$...	$+0.354^c$...	d	< 17300
NGC 1560-5	$(8.26 \pm 0.49) \times 10^{-15}$...	$+0.354^c$...	d	< 18900
NGC 1560-6	$(5.87 \pm 0.62) \times 10^{-15}$...	$+0.354^c$	8.12 ± 0.71
NGC 1560-7	$(1.47 \pm 0.29) \times 10^{-15}$...	$+0.354^c$	7.7 ± 1.3
NGC 3109-1	$(4.8 \pm 1.2) \times 10^{-16}$	$+0.15 \pm 0.57$	0	...	d	...
NGC 3109-2	$(2.47 \pm 0.17) \times 10^{-15}$	$+0.06 \pm 0.44$	0	149 ± 35
NGC 3109-3	$(4.46 \pm 0.20) \times 10^{-15}$	-0.03 ± 0.23	0	60.2 ± 2.6	14600 ± 2600	7.73 ± 0.33
NGC 3109-4	$(1.027 \pm 0.048) \times 10^{-14}$	-0.02 ± 0.29	0	25.65 ± 0.80	< 16200	> 7.62
UGC 6456-1	$(4.99 \pm 0.30) \times 10^{-15}$	-0.07 ± 0.27	0	66.1 ± 7.6	20900 ± 4000	7.21 ± 0.23
UGC 6456-2	$(2.156 \pm 0.086) \times 10^{-14}$	-0.18 ± 0.17	0	147 ± 10	17600 ± 1700	7.45 ± 0.14
DDO 187-1	$(1.937 \pm 0.072) \times 10^{-15}$	0	0	73^e	13200 ± 700	7.69 ± 0.09
DDO 187-2	$(5.88 \pm 0.28) \times 10^{-16}$	0	0	25^e

^a From $\text{H}\alpha$ and $\text{H}\beta$ measurements at OAN; see Table 12.

^b IC 10-2 (HL111c; Table 7): this value of the oxygen abundance agrees with the value independently derived by Richer et al. (2001) for the same Steward data; they obtain $12 + \log(\text{O}/\text{H}) = 8.23 \pm 0.09$.

^c Average $E(B - V)$ computed from $\text{H}\alpha$ and $\text{H}\beta$ measurements from red spectra; see Table 14.

^d Negative equivalent width, owing to negative continuum.

^e From van Zee, Haynes, & Salzer (1997).

Note. — Column (1): H II region. Column (2): $\text{H}\beta$ intensity, corrected for underlying Balmer absorption and reddening. Columns (3) and (4): Computed and adopted reddening values. Column (5): $\text{H}\beta$ emission equivalent width, corrected for underlying Balmer absorption. Column (6): Computed O^{+2} electron temperature, assuming an electron density of 100 cm^{-3} . Column (7): Derived oxygen abundance.

Table 20. Stars and gas in field dIs.

dI Name (1)	M_B (mag) (2)	$\log M_{\text{HI}}$ (M_\odot) (3)	$\log M_{\text{gas}}$ (M_\odot) (4)	$\log M_{\text{HI}}/L_B$ ($M_\odot/L_{\odot,B}$) (5)	$\log M_*$ (M_\odot) (6)	M_*/L_B ($M_\odot/L_{\odot,B}$) (7)	μ (8)	$\log \log (1/\mu)$ (9)
DDO 187	−12.72	7.32	7.46	+0.044	7.03	0.56	0.729	−0.863
GR 8	−12.19	7.04	7.17	−0.027	6.74	0.47	0.731	−0.867
Ho II	−15.98	8.93	9.06	+0.344	8.55	0.91	0.767	−0.939
IC 10	−15.85	8.14	8.27	−0.394	8.65	1.29	0.299	−0.280
IC 1613	−14.53	7.97	8.10	−0.036	8.13	1.33	0.486	−0.505
IC 2574	−17.06	9.16	9.30	+0.146	8.94	0.84	0.693	−0.799
IC 4662	−15.84	8.40	8.53	−0.132	8.30	0.58	0.632	−0.701
Leo A	−11.53	6.99	7.12	+0.186	6.45	0.44	0.813	−1.046
LMC	−17.94	8.82	8.96	−0.544	9.37	1.01	0.279	−0.257
NGC 1560	−16.37	8.85	8.98	+0.107	8.73	0.98	0.641	−0.714
NGC 1569	−16.54	7.99	8.13	−0.818	8.57	0.58	0.264	−0.238
NGC 2366	−16.28	8.95	9.08	+0.243	8.78	1.18	0.670	−0.760
NGC 3109	−15.30	8.94	9.07	+0.624	8.30	0.97	0.855	−1.168
NGC 4214	−18.04	9.24	9.37	−0.169	9.39	0.97	0.489	−0.507
NGC 5408	−15.81	8.25	8.38	−0.269	8.49	0.94	0.439	−0.446
NGC 55	−18.28	9.18	9.31	−0.326	9.52	1.04	0.383	−0.380
NGC 6822	−14.95	8.13	8.26	−0.042	8.19	1.05	0.541	−0.574
Sextans A	−14.04	8.03	8.16	+0.219	7.64	0.69	0.767	−0.939
Sextans B	−14.02	7.65	7.78	−0.150	7.73	0.86	0.530	−0.559
SMC	−16.56	8.95	9.09	+0.136	8.92	1.28	0.593	−0.644
UGC 6456	−13.90	7.90	8.04	+0.154	7.58	0.68	0.741	−0.886
WLM	−13.92	7.79	7.93	+0.033	7.65	0.78	0.652	−0.735

Note. — Column (1): Name of the dI. Column (2): Absolute magnitude in B . Columns (3) and (4): H I gas and total gas masses. Column (5): H I gas mass-to-blue-light ratio. Column (6): Stellar mass. Column (7): Stellar mass-to-light ratio in B . Column (8): Fraction of mass in baryons in the form of gas. Column (9): Inverse gas fraction, as conveyed by $\log \log (1/\mu)$.

Table 21. Sensitivity to Ingredients in the Two-Component Method.

Model	Note	Obtained Fit	RMS in $\log(\text{O/H})$ (dex)
(1)	$(M_*/L_B)_{\text{old}} = 3.11$	$\mathcal{Y} = (8.55 \pm 0.43) + (1.38 \pm 0.41)\mathcal{X}$	0.250
(2)	$(M_*/L_B)_{\text{old}} = 1.54$	$\mathcal{Y} = (8.71 \pm 0.45) + (1.19 \pm 0.38)\mathcal{X}$	0.248
(3)	$(B - V)_{\text{old}} = 0.74$	$\mathcal{Y} = (8.56 \pm 0.40) + (0.92 \pm 0.14)\mathcal{X}$	0.167
(4)	$(M_*/L_B) = 1$	$\mathcal{Y} = (8.65 \pm 0.44) + (1.16 \pm 0.32)\mathcal{X}$	0.244
(5)	$(M_*/L_B)_{\text{old}} \propto (L_{B,\text{old}})^{0.175}$	$\mathcal{Y} = (8.64 \pm 0.40) + (1.01 \pm 0.17)\mathcal{X}$	0.162

Note. — \mathcal{Y} represents the oxygen abundance, $12 + \log(\text{O/H})$, and \mathcal{X} represents $\log \log(1/\mu)$. Model (1): the mass-to-light ratio for old stars is fixed at a constant value, based upon the properties of the Milky Way disk. Model (2): the mass-to-light ratio for old stars is fixed at a constant mean value over all dIs in the sample. Model (3): the mass-to-light ratio for old stars varies with the luminosity of the old component as a power law, and the $B - V$ colour for old stars is fixed at a constant mean value over all dIs in the sample. Model (4): the mass-to-light ratio for *all* stars is fixed at unity, motivated by the Bruzual & Charlot (1996) models and the absence of any trend in $B - V$ colour with B luminosity (Lee 2001). Model (5): full two-component model (Equation (28)).